Twenty-Five Years of Background-Oriented Schlieren: Advances and Novel Applications

Bryan E. Schmidt*
Case Western Reserve University, Cleveland, Ohio 44106

Brett F. Bathel†
NASA Langley Research Center, Hampton, Virginia 23681

Samuel J. Grauer‡
Pennsylvania State University, University Park, Pennsylvania 16802

Michael J. Hargather§
Los Alamos National Laboratory, Los Alamos, New Mexico 87545

James T. Heineck¶
NASA Ames Research Center, Mountain View, California 94035

Markus Raffel‖
German Aerospace Center (DLR), 37073 Göttingen, Germany

Since its introduction in the year 2000, background-oriented schlieren (BOS) has become a cornerstone technique for visualizing variable-density flows. In this review, we provide a rigorous examination of the optical principles underpinning BOS and related refractive-index-based techniques, complemented by an appendix linking schlieren imaging to Maxwell's equations. The core sections delve into the practical aspects of BOS, with detailed discussions on image processing algorithms and critical considerations for experimental setups. We then explore recent advancements and innovations, including extensions of BOS with tomography, data assimilation, and event-based imaging. Finally, we present notable applications of BOS in challenging and unconventional environments, showcasing the method's versatility and offer inspiration for future research directions.

Nomenclature

b	=	projection scalar and vector
c	=	speed of light, m/s
d	=	displacement, pixels
D	=	integer pixel displacement, pixels
f	=	lens focal length, mm
$f_\#$	=	f-number
G	=	Gladstone–Dale constant, m^3/kg
I	=	image intensity field, a.u.
L	=	length, mm
M	=	magnification

*Assistant Professor, Mechanical and Aerospace Engineering, AIAA Senior Member.
†Research Engineer, Advanced Measurements & Data Systems Branch, AIAA Associate Fellow.
‡Kenneth Kuan-Yun Kuo Early Career Professor, Department of Mechanical Engineering, AIAA Member.
§Scientist, M-9 Shock and Detonation Physics, AIAA Senior Member
¶Physical Scientist, Experimental Aero-physics Branch, AIAA Associate Fellow.
‖Head of Department, Department of Helicopters, Institute of Aerodynamics and Flow Technology; Professor, Leibniz University Hannover. AIAA Associate Fellow.

n = index of refraction
p = pressure, atm
S = sensitivity factor, mm
T = temperature, K
Z = distance, mm
δ = sub-pixel displacement, pixels
ε = deflection angle, °
γ = regularization parameter
φ = voxel basis function
λ = wavelength of light, nm
ρ = mass density, kg/m^3

Subscripts
A = phase object–lens distance
B = background–lens distance
CC = cross-correlation
D = background–phase object distance
d = deflected image
ILS = iterative least squares
IW = interrogation window
r = reference image
sens = sensor quantity
0 = reference or vacuum quantity

I. Introduction

The word "Schliere" originates from the German colloquial language and roughly translates to a local inhomogeneity in the optical properties of a transparent medium. Such inhomogeneities can be observed in low-cost or antique window panes, where they distort the background scene behind the glass. Methods for visualizing such streaks in transparent media were first described in the 1600s by Hooke [1]. In 1859, Foucault [2] introduced a method for measuring beam deflection and converting it into brightness variations, which he used to analyze optical elements such as lenses and mirrors. This approach relied on essential components like a knife-edge and two lenses. A few years later, Toepler adapted this method to visualize compressible flow for the first time [3], and the term "Toepler's schlieren method" became widely adopted in fluid mechanics and flow measurement as a key technique for visualizing compressible effects in flows.

Schlieren phenomena can be perceived not only through brightness variations but also as apparent distortions in the features of a background scene when viewed through a spatially or temporally varying inhomogeneity. A well-known example of this is the flickering seen in the air above a hot surface. Since these effects integrate over the line of sight, such observations are particularly pronounced over long distances and in the presence of strong density gradients in the air. For instance, the dark surface of an asphalt road in summer generates sharp temperature gradients in the air above it, leading to density differences that manifest as the visible effect known as "road shimmer." This perception of background distortion is what we refer to here as the background-oriented schlieren or BOS method.

The first descriptions of the BOS principle and photographic recordings of BOS images date back to publications from the 1940s [4]. The adaptation of BOS for digital recording and analysis emerged through a flurry of developments in the year 2000. Dalziel et al. [5] published an article in *Experiments in Fluids* in April, describing several schlieren and moiré techniques collectively termed "synthetic schlieren." Some of these techniques, particularly dot tracking refractometry, are fundamentally equivalent to the BOS method. In May, Raffel et al. [6] introduced a BOS implementation using a random dot pattern background and demonstrated its application for visualizing the rotor wake of a hovering helicopter. Meier's patent application [7] followed in June. Subsequently, Richard et al. [8] presented various BOS applications at a conference in Lisbon in July, highlighting the experimental and computational requirements for quantitative density estimation. Then in August, Raffel et al. [9] further explored the conventional, reference-free, and natural background variations of BOS, laying the groundwork for airborne BOS applications.

Over the past 25 years, BOS applications and implementations have expanded significantly. While the fundamentals of the technique were reviewed by Raffel in 2015 [10], the last decade has seen considerable advancements, including

novel processing methods, enhanced tomographic and quantitative measurement techniques, and innovative uses of platforms and backgrounds. In this review, we describe the fundamentals of BOS imaging and highlight some of the most significant recent developments in this area.

II. Principles of BOS

Optical methods for determining the density field of a fluid are generally based on visualizing refractive index variations in the flow. These methods can be broadly categorized into three main types: schlieren, shadowgraphy, and interferometry. All three techniques exploit the bending, or "refraction," of light waves over gradients in the refractive index field, resulting in detectable changes in the intensities captured by an imaging system. While these diagnostic methodologies differ in their physical setups and functional dependence on the refractive index field, they share common principles. BOS is a schlieren-based technique, so our discussion focuses on the physical foundations and principles of schlieren imaging. For a comprehensive overview of all three approaches, see Settles [1].

Quantitative schlieren methods rely on a physical understanding of light propagation through inhomogeneous media. The local speed of light is determined by the microscopic properties of the medium, which are linked to macroscopic quantities of interest, such as density and the speed of light. A model of light propagation through a variable-index medium establishes the connection between these macroscopic properties and the visible distortions of the background pattern in BOS (or the changes in intensity visualized with a traditional schlieren system). While this relationship can be described using a geometric analysis of the wavefront, refraction is fundamentally an electromagnetic phenomenon. In the sections that follow, we review the simplified geometric treatment of schlieren, practical aspects of BOS imaging, and we compare BOS to traditional schlieren techniques. A brief treatment of the electromagnetic foundations of schlieren is provided in Appendix A.

A. Geometric Analysis of Schlieren

The speed of light in a transparent medium, c, is related to the speed of light in a vacuum, $c_0 \approx 3 \times 10^8$ m/s, through the refractive index,

$$n = \frac{c_0}{c}. \tag{1}$$

In general, the refractive index depends on the wavelength of light, λ, and the thermochemical state of the medium, including its density, temperature, pressure, and composition. For anisotropic media, n also varies with the direction of propagation. When the refractive index of a specific substance is known at a given wavelength and thermodynamic state, the Lorentz–Lorenz equation can be used to determine n at other states,

$$\frac{1}{\rho}\frac{n^2-1}{n^2+2} = \frac{A}{W} = \text{constant}, \tag{2}$$

where A is the wavelength-dependent molar refractivity and W is the mean molecular weight, both of which are properties of the transmission medium.

For gases, where n is nearly unity, the Lorentz–Lorenz equation can be linearized to yield the Gladstone–Dale equation,

$$n = 1 + G\rho, \tag{3}$$

where $G \approx 3A/2W$ is the Gladstone–Dale coefficient [11]. Additional details on the foundations of A and G are given in Appendix A. Relations and data to compute these coefficients for a mixture can be found in Appendix B. A typical value of G for dry air and visible light is $G = 2.26 \times 10^{-4}$ m^3/kg. Since both the Lorentz–Lorenz and Gladstone–Dale equations link the density of a gas to its refractive index, changes in n can, in theory, be used to infer changes in density or other properties that influence the refractive index, provided the remaining variables are known or controlled. For instance, refractive index measurements can be applied to estimate pressure, molar concentrations, or temperature in gaseous media. For a clear interpretation of the measured values, however, the constancy of the other variables must be inferred from known boundary conditions or additional measurements.

Refraction is often introduced using the example of a discrete interface, such as a light beam passing from air into a glass of water and then out again. As the beam transitions between these media, its speed changes, resulting in a shift in the light beam's trajectory at each interface. This bending distorts both the contents of the glass and the scene behind it. When light slows, corresponding to an increase in n, it bends toward the surface normal, as depicted in Fig. 1a. The

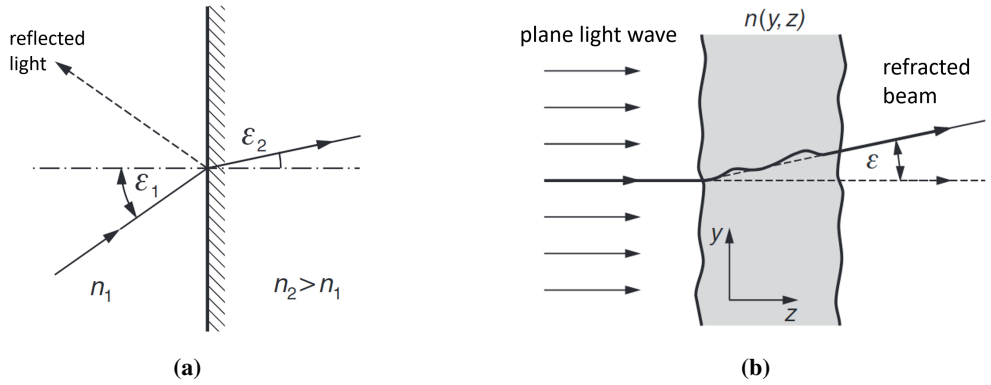

Fig. 1 Simplified diagrams of refraction: (a) Snell's-Law-type refraction and reflection at an interface and (b) light refraction through a variable-index medium.

change in the light beam's direction at the interface of two homogeneous media is governed by Snell's Law,

$$n_1 \sin(\varepsilon_1) = n_2 \sin(\varepsilon_2)\,, \tag{4}$$

where ε_1 and ε_2 are the angles of incidence and refraction, respectively, as illustrated in Fig. 1a.

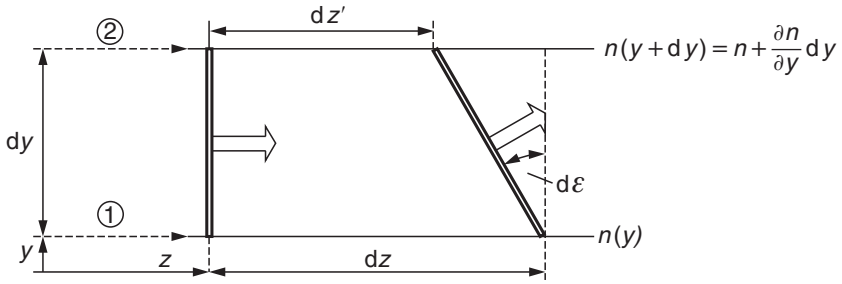

Fig. 2 Differential section, dy, of the plane wave front over the interval dt.

This principle can be generalized to media with continuously varying refractive indices. Consider a plane wave incident on such a medium, like the diagram in Fig. 1b, which represents a typical schlieren scenario. For simplicity, we analyze only two dimensions: the optical axis z and the vertical axis y, noting that the treatment for the normal axis x is identical to that of y. The distortion of a differential wavefront segment, dy, over a short interval, dt, is illustrated in Fig. 2. Using the relation $c = c_0/n$, we can express the propagation increments at the bottom and top of the wave segment, respectively, as

$$\mathrm{d}z = \underbrace{\frac{c_0}{n}}_{c(y)}\,\mathrm{d}t \quad \text{and} \quad \mathrm{d}z' = \underbrace{\frac{c_0}{n + \frac{\partial n}{\partial y}\,\mathrm{d}y}}_{c(y+\mathrm{d}y)}\,\mathrm{d}t. \tag{5}$$

The difference between dz and dz' arises from the gradient of n with respect to y. Assuming the change in n is small, we can use the binomial approximation to get

$$\mathrm{d}z' \approx \frac{c_0}{n}\left(1 - \frac{1}{n}\frac{\partial n}{\partial y}\,\mathrm{d}y\right)\mathrm{d}t. \tag{6}$$

The turning angle associated with the wavefront distortion in Fig. 2 is

$$\tan\left(\mathrm{d}\varepsilon_y\right) = \frac{\mathrm{d}z - \mathrm{d}z'}{\mathrm{d}y} = \frac{c_0}{n^2}\frac{\partial n}{\partial y}\,\mathrm{d}t = \frac{1}{n}\frac{\partial n}{\partial y}\,\mathrm{d}z, \tag{7}$$

For small turning angles, $\tan(\mathrm{d}\varepsilon_y) \approx \mathrm{d}\varepsilon_y$, and since n is *nearly* unity throughout the gas, $n \approx n_0$, where n_0 is the ambient refractive index. Applying these simplifications, we obtain

$$\mathrm{d}\varepsilon_y = \frac{1}{n_0}\frac{\partial n}{\partial y}\mathrm{d}z. \tag{8}$$

The total deflection angle in the y-direction, ε_y, is determined by integrating $\mathrm{d}\varepsilon_y$ along the light path,

$$\varepsilon_y = \frac{1}{n_0}\int \frac{\partial n}{\partial y}\,\mathrm{d}z. \tag{9}$$

Thus, if the refractive index field is known as a function of three-dimensional space, the deflection angle can be calculated. A similar derivation yields an analogous expression for ε_x, with $\partial n/\partial x$ replacing $\partial n/\partial y$. While the deflection vector $\underline{\varepsilon} = (\varepsilon_x, \varepsilon_y, \varepsilon_z)$ is a 3D quantity, only the components normal to the sensor plane, i.e. x and y, can be resolved in each measurement.

B. BOS Measurements

In BOS, a camera focuses through the working fluid onto a background plane featuring a visible pattern. When the flow is quiescent, light passes through the domain without refracting, producing a clean "reference" image of the background. Once the flow is activated, density gradients introduce phase disturbances, as described by the relations derived in the previous section. These disturbances refract the light, creating "deflected" (or distorted) images of the pattern. As a result, the flow is commonly referred to as the *phase object*, which is a general term used in schlieren imaging for a medium of interest that distorts light rays and could refer to a solid object such as a lens.

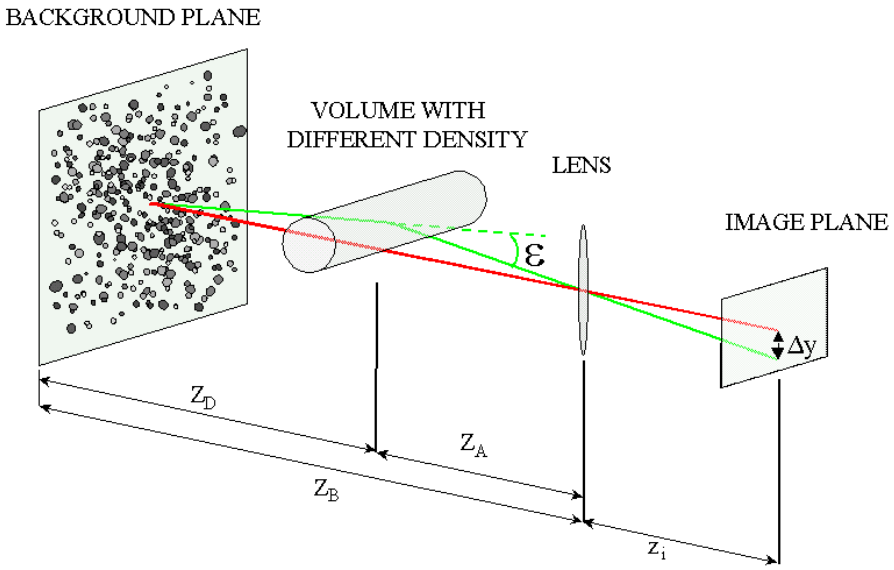

Fig. 3 Sketch of BOS imaging [12]. Image used with permission of the authors.

A basic single-camera BOS setup is illustrated in Fig. 3. The optical axis z is perpendicular to the sensor (image plane), the deflection produced by the phase object, and the background plane. The physical (x, y) directions align with the camera's horizontal u-axis and vertical v-axis, respectively. Two rays originate from the same feature on the background. The straight red ray corresponds to the reference condition, where the medium is at rest and no phase disturbance is present. This ray intersects the sensor at the pixel location (u, v). Later, the flow is activated and the bent green ray is refracted by the fluid, undergoing a turning angle ε_y, and intersects the sensor at a displaced location $(u, v - \delta_v)$. World coordinates are generally represented as $\underline{x} = (x, y, z)$, sensor coordinates as $\underline{u} = (u, v)$, and the vector deflection field produced by refraction as $\underline{\delta} = (\delta_u, \delta_v)$. For quantitative applications, a camera transform and its inverse are required to map between $\underline{x}$ and $\underline{u}$, enabling conversions between world coordinates and sensor coordinates.* Once

*It is worth noting that the transform becomes straightforward for single-camera imaging of an axisymmetric flow when using a long focal length lens and an axis-aligned setup, as depicted in Fig. 3.

the reflected and deflected images have been acquired, the two-dimensional deflection field $\underline{\delta}$ can be determined using one of several types of algorithms. A complete discussion of processing algorithms is provided in Sec. III.

It is interesting to note here that the BOS technique shares many common features with so-called "density speckle photography" (DSP), as described by Debrus et al. [13] and Köpf [14], and in a further improved version by Wernekinck and Merzkirch [15]. As with laser interferometry, the laser-based DSP method uses an expanded coherent laser beam to illuminate the phase object and visualize the variation of the refractive index. In contrast to interferometry, however, DSP does not generate interference fringes but analyzes the offset of the laser speckle pattern formed on a ground glass screen on the opposite side of the phase object from the camera and laser. Comparing the sketch of the BOS technique in Fig. 3 with representations of the DSP technique reveals that these methods appear to be largely identical, as is the post-processing strategy. However, two significant differences can be highlighted. Instead of using a laser beam and diverging optics in DSP, any background can be used that has a sufficiently high contrast and spatial frequency for BOS. For example, this could be the printout of a random dot pattern or a layer of gravel or asphalt in the open countryside. This results in significantly reduced effort when using the BOS method. The second major difference is that in BOS the optical path over which the density gradients are measured is divergent. This can lead to a clear disadvantage of BOS compared to DSP, but is only of minor influence if a sufficiently large distance can be established between the camera and the background. The use of a divergent optical path does not represent a disadvantage for potential tomographic evaluations either, since methods based on the numerical calculation of convolution integrals have been known for some time for the evaluation of divergent images as described in Sec. V.A.

The magnitude of displacements observed in BOS depends on both the experimental setup and the fluid and flow properties. Key distances in the setup include the background-to-phase object distance z_D, the phase object-to-lens distance z_A, and the total background-to-lens distance $z_\mathrm{B} = z_\mathrm{A} + z_\mathrm{D}$. The distance from the lens to the sensor is z_i. Pixels on the sensor have a pitch ψ (reciprocal length), and the lens has a focal length f. These parameters define the image magnification,

$$M = \frac{f}{z_\mathrm{B} - f}. \tag{10}$$

Deflections are assumed to originate from a discrete point, typically at the mid-plane of the phase object. Outside the phase object, refractive index gradients are assumed negligible, so light rays travel in straight lines from the background to the flow domain, where they can be refracted before continuing straight towards the lens. Using these assumptions, the u- and v-direction deflections on the sensor, measured in pixel units, are given by

$$d_u = \psi M z_\mathrm{B} \varepsilon_x \quad \text{and} \quad d_v = \psi M z_\mathrm{B} \varepsilon_y. \tag{11}$$

In other words, the deflection field $\underline{\delta}$ is directly proportional to the product $M z_\mathrm{B}$. However, the phase object must remain in the camera's effective depth of field as z_B increases and it remains focused on the background pattern. This introduces a complex set of trade-offs in the experimental design, which are discussed in detail in Sec. IV.

The deflection vector is effectively a line-of-sight convolution of the refractive index gradient. In vector form, it is expressed as:

$$\underline{\varepsilon} = \frac{G}{n_0} \int \nabla\rho \, \mathrm{d}s, \tag{12}$$

where the components of $\underline{\varepsilon}$ normal to the sensor plane can be determined through deflection sensing, as described in Sec. III. For axisymmetric flows, their 2D nature allows the density field to be reconstructed from a single perspective. However, for more general 3D flows, BOS measurements must be acquired from multiple perspectives, and a 3D tomographic reconstruction algorithm is required to deduce ρ. This topic is further discussed in Sec.V.

To briefly illustrate issues of sensitivity and spatial structure, consider a radially symmetric Gaussian refractive index field, as depicted in Fig. 4. The refractive index phantom shown in Fig. 4a represents an idealized 2D compressible vortex, with a peak refractive index variation of 0.015% relative to the ambient value.[†] The resulting ray deflections are plotted against v over a distance of five dimensionless length units in Fig.4b. Despite the unambiguous relationship between δ_v and n for this phantom, the spatial structures of these quantities differ. Specifically, using the Leibniz integral rule, $\delta_v \propto \nabla\bar{\rho}$, where

$$\bar{\rho} = \int \rho \, \mathrm{d}s, \tag{13}$$

is the projected density (see Ref. [16]). Consequently, recovering $\bar{\rho}$ requires solving the Poisson equation obtained by taking the divergence of d_v, i.e. $\underline{\nabla} \cdot d_v = \nabla^2\bar{\rho}$, or a similar mathematical problem. Additionally, the small magnitude of d_v means that estimates are particularly vulnerable to image noise and errors in the deflection sensing algorithm.

[†]Note that the minimum refractive index occurs in the center of the Gaussian.

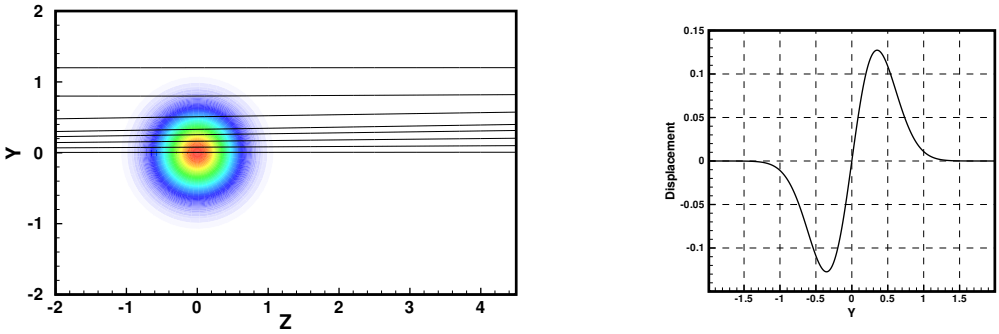

(a) (b)

Fig. 4 Simulation of BOS data: (a) light trajectories through a Gaussian density field (minimum density at the center) and (b) computed displacement of light rays at $z = 5$.

C. Comparison to Traditional Schlieren Imaging

BOS and traditional schlieren methods both yield images of refractive index gradient fields which can be considered optically equivalent. Examining the experimental setups of each technique shows that the light ray paths, and distortions recorded, are nearly identical [17]. The uniqueness of the BOS method is in the digital image processing used to reveal the distortions, ability to implement it without any sophisticated optics, and applicability to extremely large fields of view.

Traditional schlieren imaging with a knife-edge cutoff records the refractive index gradient in the direction perpendicular to the knife-edge orientation [1]. The knife-edge cutoff orientation is generally chosen to yield schlieren sensitivity in the direction of primary density, or refractive index, gradient of interest. Thus for studying a candle plume for example, the knife-edge cutoff should be vertically aligned to best image the refractive index variation horizontally across the plume. This orientation is ideal for the laminar region of the plume, but limits visibility in the turbulent regions where light refractions are oriented in multiple different directions. A horizontal knife-edge cutoff could be utilized instead, or added in parallel using a beamsplitter and second camera [18], to record the vertical light ray deflections. This second cutoff adds system complexity and/or cost. Other cutoff geometries including circular apertures [1] or color rainbow cutoffs [19] can yield refraction measurement in other directions or magnitudes, but still must be chosen *a priori*. The cutoff choice sets the schlieren imaging result, whereas the BOS technique records the vector light ray deflection within the imaging plane, which can then be post-processed to any direction.

This is a primary benefit of the BOS system: the vector direction and magnitude of a light ray refraction is recorded everywhere in the image. A single BOS image can be presented as a vertical knife-edge cutoff schlieren image by plotting the measured horizontal pixel displacements d_u, or as a horizontal knife-edge cutoff schlieren image by plotting the vertical pixel displacements d_v. Additional images with arbitrary cutoff direction can be easily produced through post processing. Quantitative analysis to determine the refractive index or density field is simplified also because the vector refraction was measured.

The simplicity of the BOS setup is another benefit over traditional schlieren methods. Successful BOS requires only a camera and a background with sufficient patterning. The choice of camera lens sets the field of view, which can range from microscopic to essentially arbitrarily large. The ability to image refractive disturbances on large scales with no sophisticated lenses or optics is particularly useful, as traditional schlieren methods have always been limited by the scale of optics available. Lens-and-grid schlieren methods were developed to perform large-scale imaging up to several meters in a warehouse building [20] and in a telescope [21, 22] implementation. Both of these required a background "edge," either the edge of a retroreflective strip [20] or the edge of the sun [22], which was then aligned with a cutoff in front of the camera to produce the schlieren system. The BOS method has eliminated the need for these sharp edges and cutoffs through digital image processing, allowing full-field imaging at any scale as long as some background patterning exists [23].

Compared to traditional schlieren, BOS has two primary disadvantages which are the non-parallel light arrangement and the need for image processing. The non-parallel light arrangement in BOS, as discussed above, can result in some degree of blurring of the surfaces of objects imaged with BOS because the subject in sharp focus is the background pattern, not the phase object. This can be limited by the choice of camera lens and geometry of the setup, essentially

by maximizing the depth of field of the imaging system. The non-parallel arrangement also can cause challenges with measuring refractions near the surfaces of objects and requires geometric corrections for measuring the physical dimensions of features located in different planes.

The image processing required to produce a BOS image adds the need for post-processing and can limit the final image resolution. Traditional schlieren systems yield real images which are imaged with a camera directly. This enables live images or videos of the schlieren images which can be useful for experiments and adjusting parameters such as cutoff and alignment on the fly while examining the output images. BOS requires post-processing to produce the images, so the effectiveness of the setup is not necessarily known during setup, unless a real-time algorithm is employed as discussed in Sec. III.A. Careful planning and background feature size choices are required to ensure quality BOS images can be produced. The BOS post-processing algorithms manipulate the recorded pixel intensities to produce the BOS images and data, which can result in averaging or loss of resolution depending on the algorithm that is used for the processing (see Sec. III).

III. Deflection Sensing Algorithms

As mentioned in the previous section, unlike traditional schlieren imaging, BOS requires an image processing routine of some kind in order to produce schlieren images. A simple but fast approach that gives a rough indication of the types of features that will be visible is simply to subtract the deflected image from the reference image. To obtain a proper schlieren image, however, a more sophisticated algorithm is required to determine the two-dimensional displacement field $\underline{\delta}(\underline{u})$ at pixel locations $\underline{u}$ that accounts for the difference between the deflected image I_d and the reference image I_r due to refraction. Under stable lighting conditions, this is represented by

$$I_\mathrm{r}(\underline{u}) = I_\mathrm{d}(\underline{u} + \underline{\delta}(\underline{u})) \tag{14}$$

This amounts to an *image registration* problem [24], which is a classical inverse problem in mathematics, or equivalently to an *optical flow* problem [25] where the displacement between images is not interpreted as velocity. Both of these are ill-posed, in the sense that there are more unknowns (two components of a vector field) than equations (intensity values at each pixel). Other measurement techniques in science engineering whose development predate BOS, specifically particle image velocimetry (PIV) and digital image correlation (DIC) involve the exact same mathematical problem, and therefore the algorithms developed for those applications can be readily used for BOS as well. These include cross-correlation (CC), iterative least squares (ILS), and optical flow (OF), which are addressed in this section. One additional recent technique that can be applied when the background pattern is periodic, Fourier demodulation, is also included. The methods are compared using test images in Figs. 5 and 6.

In practice, the choice of algorithm is secondary to other factors, such as the selection of the background pattern and the details of the setup. Numerical experiments in the literature have shown that while the algorithm has an effect on accuracy and spatial resolution, the advantages of a higher-fidelity algorithm such as OF are primarily realized for flows where small-scale structures are prevalent and the images are essentially noise-free [26, 27]. Even then, the defocusing effect discussed in Sec. IV.B can render these advantages moot by washing out the fine flow scales. Furthermore, the background pattern itself must also contain small features such that the distortions can be detected in the first place.

A. Cross-Correlation

The first algorithm to be applied to process BOS images was cross-correlation (CC) [5, 6], which is commonly used for PIV processing. CC involves dividing the images into interrogation windows, which are typically 8-16 pixels square and overlapped by 50%, and then correlating the intensity distribution in each window across the reference and deflected images either directly or in the Fourier domain. Small interrogation windows are preferred for BOS because the displacements are typically only a few pixels, and smaller interrogation windows result in higher spatial resolution. The cross-correlation operation is performed in the Fourier domain, which makes it highly computationally efficient. Because CC algorithms used for BOS were developed for PIV, they are often paired with a background pattern consisting of random dots to emulate tracer particle images encountered in PIV. Rajendran et al. [28] developed an explicit dot-tracking method for random-dot backgrounds that performs favorably compared to CC at increased computational cost.

There are two key differences between typical BOS and PIV images that have motivated the use of other algorithms besides CC. First, the inter-frame displacements encountered in BOS are typically quite small compared to PIV, on the order of a few pixels instead of 10–20 pixels. This means that the advantages of CC for dynamic range and capacity

to resolve large displacements are largely wasted in BOS applications, at the cost of reduced accuracy and resolution compared to other methods. Second, while PIV algorithms are optimized for images of discrete tracer particles, the user is free to choose any pattern for BOS, and the ideal pattern for resolving a general displacement field is not discrete points of localized brightness [26, 27].

1. GPU Processing

One of the chief advantages of CC compared to other methods is its computational efficiency, which in many cases can outweigh a potential reduction in accuracy or resolution, especially if those gains are minimal due to other factors. Because the computation of cross correlations in the Fourier domain can be performed using parallelized routines on GPUs, the computational speed can be decreased even further, and by a significant margin. Wernet implemented an FFT-based CC method on GPUs, and demonstrated a processing time of 162 images per second on 5 megapixel images, with a final interrogation window size of 8×8 pixels with 50% overlap [29]. This means that the BOS images can be processed in real-time during acquisition, and hence the algorithm is referred to as "real-time BOS" (RT-BOS). Real-time processing alleviates a significant drawback of BOS compared to conventional schlieren, namely that the schlieren images cannot be viewed easily during setup to permit making adjustments to the system because they must be processed off-line. RT-BOS is therefore an extremely valuable tool for optimizing a BOS setup, even if another algorithm is to be used later to perform final processing of the images.

2. Ensemble Methods

In cases where the image acquisition rate is significantly faster than the fluctuations in the flow field, the image quality and effective resolution can be significantly improved by using a sliding average, which tends to cancel out random fluctuations resulting from processing images containing noise. While this can be performed for BOS images obtained from any processing algorithm, CC offers a particular advantage in this respect. Meinhart et al. demonstrated that averaging the correlation maps prior to determining displacement vectors at an intermediate step during CC processing significantly increases the accuracy of time-averaged velocity fields in PIV compared to averaging after computing vector fields [30]. Raffel et al. applied the same strategy to BOS images, and obtained ensemble-averaged CC images comparable to averaged images processed with OF [31].

B. Iterative Least Squares

The need to determine sub-pixel displacements more accurately than what is possible using CC in DIC applications motivated the development of the iterative least squares (ILS) method [32]. The estimation of sub-pixel displacements with CC involves the interpolation of the cross-correlation function for each interrogation window, which as affected by the shape of the peak and can introduce errors. In ILS, sub-pixel displacements $\underline{\delta}_\mathrm{s}$ are computed using a separate procedure after determining the integer-pixel displacements $\underline{\delta}_\mathrm{p}$ using CC. This is done by decomposing the displacements $\underline{\delta}$ into

$$\underline{\delta} = \underline{\delta}_\mathrm{p} + \underline{\delta}_\mathrm{s} \tag{15}$$

The sub-pixel displacements are computed using a technique similar to the block-matching OF algorithm of Lucas and Kanade [33], except it allows for linear illumination changes between I_r and I_d [32]. Equation (14) is modified to

$$aI_\mathrm{r}(\underline{u}) + b = I_\mathrm{d}\big(\underline{u} + \underline{\delta}_\mathrm{p}(\underline{u}) + \underline{\delta}_\mathrm{s}(\underline{u})\big) \tag{16}$$

where a and b are unknown constants representing the illumination change. Equation (16) is then solved using a first-order Taylor expansion at each pixel location $\underline{u}_i$.

$$aI_\mathrm{r}(\underline{u}_i) + b = I_\mathrm{d}\big(\underline{u}_i + \underline{\delta}_\mathrm{p}(\underline{u}_i)\big) + \nabla I_\mathrm{d}\big(\underline{u}_i + \underline{\delta}_\mathrm{p}(\underline{u}_i)\big) \cdot \underline{\delta}_\mathrm{s}(\underline{u}_i) \tag{17}$$

The spatial derivatives in Eq. (17) are computed using finite differences, and the equation is then solved via linear least squares for a neighborhood of pixels around $\underline{u}_i$, typically 3×3 or 5×5 pixels, assuming that $\underline{\delta}_\mathrm{p}$ is the same for all pixels in that neighborhood. The ILS method has been shown to possess higher accuracy for sub-pixel displacements and lower sensitivity to the details of the background pattern and imaging noise compared to CC [34], and has therefore been implemented in popular commercial BOS algorithms. There are now also commercial ILS-based algorithms that have a real-time BOS measurement capability similar to that of GPU-accelerated CC-based processing [29].

C. Optical Flow

In contrast to CC and ILS which solve for displacements locally for each interrogation window or pixel neighborhood, respectively, optical flow (OF) methods solve Eq. (14) globally for the entire image domain. The resulting displacement field has one vector at every pixel, although the actual effective spatial resolution is not exactly one pixel because neighboring pixels are correlated by regularization. OF methods solve Eq. (14) using a variational approach by forming a minimization problem of the form

$$\hat{\underline{\delta}} = \arg\min_{\underline{\delta}} \mathcal{J}_\mathrm{D}(I_\mathrm{r}, I_\mathrm{d}, \underline{\delta}) + \gamma\, \mathcal{J}_\mathrm{R}(\underline{\delta}) \ . \tag{18}$$

Here, $\mathcal{J}_\mathrm{D}$ is a penalty function formed from Eq. (14) and $\mathcal{J}_\mathrm{R}$ is a regularization term that enforces smoothness on the solution. The two terms are weighted by a scalar parameter γ that must be selected by the user. Several formulations of $\mathcal{J}_\mathrm{R}$ appear in the literature, from first-order Tikhonov regularization in the classical algorithm of Horn & Schunck [23, 25, 26, 31, 35] to higher order derivatives such as the Laplacian operator [27]. It should be noted that the arguments of $\mathcal{J}_\mathrm{D}$ and $\mathcal{J}_\mathrm{R}$ are field variables, with scalar fields I_r and I_d and the vector field $\underline{\delta}$.

Comparative studies in the literature, particularly those of Atcheson et al. [26] and Schmidt & Woike [27], have consistently shown that OF produces the most accurate displacement fields compared to CC and ILS for idealized synthetic images, and can reveal finer-scale structures depending on the flow field and background pattern used. However, the cost in terms of processing time can be significant. OF methods can require more than an order of magnitude longer to process the same image pair compared to CC, GPU acceleration notwithstanding, which can be meaningful for large data sets or high-resolution images.

D. Fourier Demodulation

Very recently, Wildeman introduced a completely different strategy for BOS processing based on Fourier demodulation that does not solve Eq. (14) in a traditional sense like the previously described methods, dubbed "Fast Checkerboard Demodulation (FCD)" [36]. The method operates on the same principle as frequency modulation (FM) radio transmission, where a high frequency periodic "carrier" is phase-modulated by a signal. Reconstruction is a straightforward matter of determining the phase shifts in the Fourier domain, which are centered around the carrier peak. In the context of BOS, if the background is periodic with a high spatial frequency, such as a two-dimensional sinusoid or a checkerboard pattern, then the same procedure can be applied to determine the two-dimensional phase shifts, which is the displacement field $\underline{\delta}$. Because the spatial frequency of the undisturbed background is uniform in space, the problem is no longer mathematically ill-posed and can be solved directly and efficiently in the Fourier domain using simple filtering.

Wildeman shows that in order to resolve the flow features adequately and avoid phase wrapping, the following criteria must be met [36].

$$\frac{k_\mathrm{s}}{k_\mathrm{c}} < \frac{1}{\sqrt{2}} \tag{19}$$

$$k_\mathrm{s}|\underline{\delta}| < \frac{1}{\sqrt{2}} \tag{20}$$

$$k_\mathrm{c}|\underline{\delta}| < \pi \tag{21}$$

Here, k_s is the maximum wavenumber of the flow to be resolved and k_c is the wavenumber of the background pattern. In practice, it is typically not difficult to design a background pattern that satisfies these criteria [37]. While FCD imposes restrictions on the background pattern to be used that would prevent its use in certain situations such as imaging with natural backgrounds, the benefits are significant when a periodic pattern can be employed. The processing time is much shorter even than CC, and Vinnichenko et al. found specifically that FCD is 3-5 times faster than CC and two orders of magnitude faster than OF [38]. In the same study, they showed that FCD has better overall accuracy on synthetic images than OF or CC as well, although extra care must be taken at image boundaries or in the presence of occlusions to prevent the production of artifacts [36].

E. Comparison of Algorithms

Detailed, quantitative comparisons of various processing techniques can be found in several published articles, e.g. Refs. [26, 27, 31, 38]. Here, a brief comparison is made to demonstrate the performance of the four algorithms described in this section. The test BOS image was created by performing a ray-tracing calculation through a density field from a

simulation of buoyancy-driven turbulence from the Johns Hopkins Turbulence Database [39, 40] with a lens f-number $f_\#$, i.e. the ratio of the lens focal length to the aperture, of 8. The reference image is 1024×1024-pixel noise blurred with a Gaussian filter with a width of 2 pixels, and is shown in Fig. 5a. The ground truth vertical displacement is shown in Fig. 5b and c, where frame c shows a zoomed-in view of the region marked by the red square in frame b. Note that a sinusoidal background with a period of 20 pixels is used for FCD processing, because a periodic pattern is required.

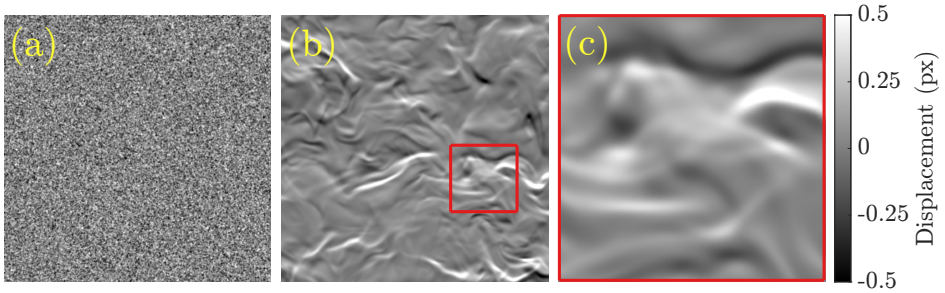

Fig. 5 Simulated data for comparing BOS processing algorithms. (a) Reference image, (b) Ground truth vertical displacement, (c) Vertical displacement in the area indicated by the red square in (b).

The results from processing the synthetic images are shown in Fig. 6. CC results were processed using an open-source algorithm commonly used for PIV [41] with 8×8-pixel interrogation windows with 50% overlap. The ILS results were computed with a commercial algorithm with a final sub-region size of 27 pixels square, and the OF algorithm was the wavelet-based method of Schmidt and Woike [27]. The settings of all algorithms, including the interrogation and sub-region sizes for CC and ILS, respectively, were optimized to minimize the total error between the computed displacement field and the ground truth. The CC and ILS results exhibit the typical sub-sampling of the displacement field, which can result in slight underestimations of the displacement magnitude in regions with sharp gradients. As the image data is noise-free, the OF and FCD results are essentially identical to one another and indistinguishable from the ground truth in Fig. 5b and c, and show superior accuracy and spatial resolution to the other methods.

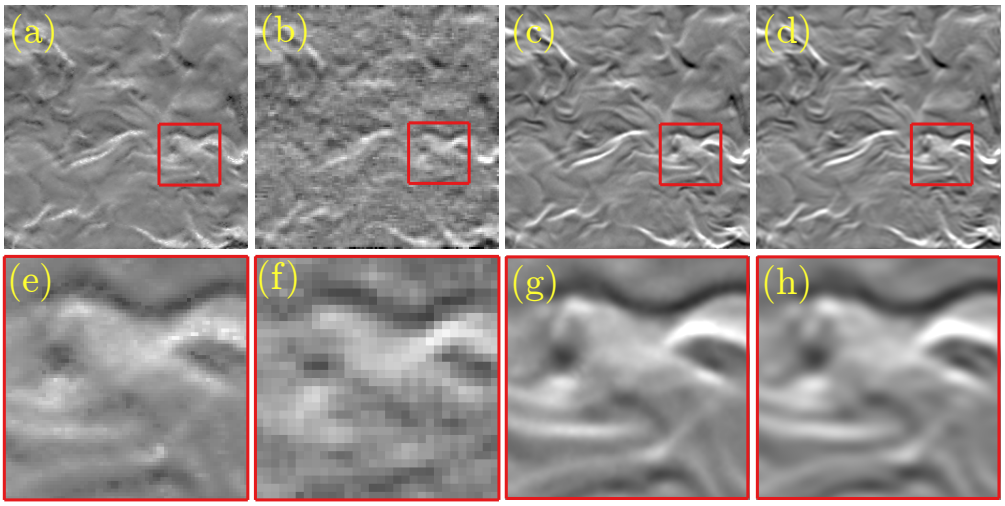

Fig. 6 Synthetic BOS images processed with (a)/(e) CC, (b)/(f) ILS, (c)/(g) OF and (d)/(h) FCD. The bottom row shows the region indicated by the red square in the top row.

IV. Optimising Setups in Practice

As described above, the evaluation of BOS image data results in a displacement field. Whether the investigated phase object can be detected in the displacement field depends on both the magnitude of the displacement and the spatial resolution at which the object is sampled. These two quantities are significantly influenced by the sensitivity and the

geometric blur provided by the setup. The following analysis of the effect of the recording parameters to be optimized follows a description described by Schwarz & Braukmann [42].

A. Sensitivity

From Eq. (11), the image displacement can be quantified as follows

$$\delta_v = f\left(\frac{z_\mathrm{D}}{z_\mathrm{D} + z_\mathrm{A} - f}\right)\varepsilon_y = S\varepsilon_y, \tag{22}$$

which depends on the deflection angle ε_y inherent to the density object, as well as the geometric and optical parameters of the setup. These consist of the focal length of the lens f, the distance between the object and background z_D, and the distance between the lens and density variation z_A (see Fig. 3). The experiment-related parameters can be summarized in the specific sensitivity factor

$$S = f\frac{z_\mathrm{D}}{z_\mathrm{D} + z_\mathrm{A} - f} \tag{23}$$

In various publications, the general conclusion is drawn that sensitivity can be increased by increasing the focal length and positioning the object closer to the camera [10, 16, 43–45]. It is generally observed that the extent to which the object can be brought closer to the camera is limited by the need to maintain the object in reasonable focus while keeping the plane of best focus on the background pattern. This introduces another trade-off involving the $f_\#$ of the lens. Higher $f_\#$ (smaller aperture) produces a larger depth of field which can allow for increased sensitivity while maintaining focus, but at the extent of decreased illumination of the sensor. However, the size of the field of view (FoV) is often a predefined boundary condition in experiment planning. The focal length needed to achieve a specific FoV size, L_FoV, at a distance z_A with a camera sensor size L_sens can be calculated as follows

$$f = \frac{L_\mathrm{sens} z_\mathrm{A}}{L_\mathrm{FoV} + L_\mathrm{sens}}. \tag{24}$$

For non-square camera sensors, either the horizontal (x, u) or vertical (y, v) extensions of the FoV and sensor must be considered. For simplicity, we will not distinguish between these different axes here. By combining Eqs. (23) and (24), a relationship can be derived, which is rarely explicitly stated (see e.g. Hargather and Settles [45]). With a fixed L_FoV and a given setup length $z_\mathrm{B} = z_\mathrm{A} + z_\mathrm{D}$, a variation of z_A leads to maximum sensitivity S at $z_\mathrm{A}/z_\mathrm{B} = 0.5$. When the setup length z_B is increased at a constant ratio of $z_\mathrm{A}/z_\mathrm{B}$, higher focal length lenses are required, leading to a higher sensitivity factor S.

B. Spatial Resolution

The two main factors limiting the spatial resolution of BOS measurements are the geometric blur of the captured schlieren object and the choice of processing algorithm, as well as the settings used for the selected algorithm. Processing algorithms are discussed in detail in Sec. III, and further details on the optimal settings for a given algorithm can often be found in the documentation in the case of a commercial algorithm or in published works e.g. Refs. [43, 44]. Therefore, this section focuses on the geometric blur resulting from the imaging setup.

Geometric blur of the captured schlieren object is inherent to the BOS technique, and is a key factor in the achievable resolution of a BOS image–often more important than effects from the processing algorithm in practice. It is often argued that the imaged object must be kept sufficiently sharp. However, a quantitative discussion of this effect is found in only a few publications [10, 44]. Rajendran et al. [28] recently provided a ray-tracing tool for generating synthetic BOS images of a dense object, which allows the effect of geometric blur to be predicted given the parameters of an imaging setup. Since such methods are computationally intensive, a rough estimate of image blur before setting up an experiment is often useful. In traditional photography, image blur is indicated by the "circle of confusion" (CoC) [46], describing the point of blur created in the camera's image plane by an imaged singular point. Typically, a maximum allowable CoC size is used to determine the depth of field (DOF) for a camera setting.

The equations of Greenleaf [46] can be used to determine the resulting CoC for a captured schlieren object at a distance z_D from the focal plane in reverse:

$$\mathrm{CoC} = \frac{f^2 z_\mathrm{D}}{f_\# z_\mathrm{A}\left(z_\mathrm{A} + z_\mathrm{D} - f\right)} \tag{25}$$

This size corresponds to the geometric blur specified in another formulation by Raffel [10]. The circle of confusion is proportional to the reciprocal of the $f_\#$ and increases with the square of the focal length f. The CoC size, and thus the blur of a captured schlieren object, is linearly related to the sensitivity S of the setup. For a given sensitivity S of a setup, $f_\#$ is the most important parameter enabling a change in the minimum size of the resolvable feature. This means that the ratio of z_A/z_B itself is not a measure of object blur, as the same sensitivity S and thus the same size of the circle of confusion (with a given $f_\#$) can be achieved with a different combination of z_A/z_B and focal length f.

When analyzing the spatial resolution of BOS measurement systems and the achievable accuracy, the relationship between the sensitivity of an experimental setup S and the inherent geometric blur that "smears" the signal, thereby limiting both the spatial resolution and the maximum achievable signal, is of particular importance. The sensitivity of a BOS setup is maximized–assuming the pinhole camera model–with a fixed FoV when the object is positioned halfway between the camera and background. Furthermore, sensitivity is directly linked to the geometric blur with which the object is captured. An increase in sensitivity S leads to a proportional increase in geometric blur when the $f_\#$, FoV, and sensor size (L_{sens}) are held constant. For the same achieved value of sensitivity, an identical BOS signal is generated, regardless of the combination of geometric and lens parameters chosen. The minimum flow feature size that can still be resolved by a BOS system has been determined by Schwarz & Braukmann [47], it is found to correspond to approximately 50% of the CoC size in the object area. The principles discussed in this section can be used to develop a stepwise method for setting up a BOS experiment to achieve a maximum signal.

V. Extensions: Tomography, Data Assimilation, and Event-Based Imaging

The methods discussed so far yield quantitative deflection fields from pairs of reference and deflected BOS images. While this is a crucial step toward determining the ultimate quantities of interest, such as the density field or other fields like velocity or partial pressures, additional processing is required to extract these quantities. In most cases, this processing involves tomographic reconstruction or, increasingly, comprehensive data assimilation.

Tomography is a computationally-enhanced sensing technique that combines line-of-sight "projections" of an unknown target function to estimate that function through a process known as "reconstruction." In the context of BOS, the projections are the deflection fields recorded from one or more perspectives, and the target function is typically the density field or refractive index field, depending on the application. While BOS tomography traditionally reconstructs only one of these fields, data assimilation extends this process by integrating additional physical models into the reconstruction algorithm. These models can be used to infer multiple fields by incorporating constraints from the compressible Navier–Stokes equations, an equation of state, advection–diffusion equations, a kinetic mechanism, and so forth. Reconstructions based on data assimilation offer a way to synthesize BOS data with these governing equations to produce more comprehensive estimates of flow properties. Tomographic reconstruction and data assimilation are discussed further below in the context of 2D and 3D BOS measurements. A third recent innovation involving the use of event-based imaging for BOS is discussed at the end of this section.

A. BOS Tomography

While the earliest demonstrations of BOS focused on quasi-planar flows [5, 6], tomographic applications have been explored since its inception. In the mid-2000s, Venkatakrishnan et al. [48, 49] used a single-camera setup to measure deflections in a Mach 2 flow over an axisymmetric cone-cylinder. Because this flow was fundamentally 2D, an Abel inversion could be applied to recover the density field from the deflection data (projections); Venkatakrishnan and coworkers successfully estimated the axisymmetric density field.[‡] Numerous demonstrations of axisymmetric BOS tomography soon followed [50–52]. However, the data from a single-camera setup are inherently ambiguous for general, non-axisymmetric 3D flows. To reconstruct such flows, therefore, several imaging orientations must be employed in tandem.

An instantaneous flow field can be reconstructed using images synchronously captured from multiple viewpoints, whereas time-averaged reconstructions can be obtained from asynchronously recorded BOS data. In 2007, Goldhahn & Seume [43] achieved steady 3D reconstructions of a twin-jet flow using a "rotisserie"-style experiment, in which the jet nozzle assembly was rotated to build up a set of projections with a fixed camera assembly. Later, in 2008, Atcheson et al. [53] demonstrated high-fidelity *instantaneous* reconstructions of the hot plume above a candle flame and a camping

[‡]Instead of using an Abel inversion, Venkatakrishnan et al. [48, 49] applied a standard tomographic reconstruction technique known as filtered backprojection, mentioned in Sec.V.B.1. To enforce axisymmetry, they assigned identical projection data to all views, although only a single view was recorded in their experiments.

stove, employing a suite of 16 machine-vision cameras. The success of this approach ignited significant interest and spurred rapid advancements in BOS tomography.

It is worth noting that the use of tomographic methods in combination with schlieren or interferometric imaging predates the advent of BOS [19, 54, 55]. Indeed, many of the techniques now commonly used in BOS tomography were adapted from earlier schlieren methods (as well as other tomographic modalities). However, BOS stands out due to its simplicity, cost-effectiveness, robustness, and ability to achieve a large field of view. The relatively basic setup allows for a large number of vantage points in BOS tomography, with up to 28 cameras being used in a single system [56]. Reconstruction accuracy is a strong function of the number of views, which motivates such efforts. These characteristics make BOS uniquely suited for tomographic imaging, helping to establish it as the dominant modality among tomographic schlieren diagnostics.

B. Tomographic Reconstruction for BOS

All tomography involves the inversion of a forward measurement model to estimate a target field from a set of projection data. In BOS, this model is derived from the deflection vector equation: the measured vector at each pixel may be converted into a turning angle, which is then related to the refractive index or density field using Eq. (12) [57]. Alternatively, BOS models can describe the deflections projected onto the background plane (as opposed to the turning angle) using a 3D version of Eq. (11) [58], or they can combine this model with the optical flow equation to form a "unified" model that directly links the refractive index (or density) field to the imaged intensity field [35, 59]. Regardless of the formulation, the model establishes the relationship between the unknown field of interest and the observed projection data, allowing the field to be reconstructed through inversion.

The BOS tomography workflow, illustrated in Fig. 7, consists of three key steps: deflection sensing, tomographic reconstruction, and solving a Poisson equation. These steps can be addressed sequentially in indirect methods, which solve each problem separately, or combined in direct methods, which merge tomographic reconstruction with the Poisson solver. Alternatively, unified methods consolidate all three steps into a single process. While these approaches are applicable to both axisymmetric and general 3D tomographic problems, as demonstrated in the works of Xiong, Sipkens, Molnar, and collaborators [60–62], the focus here is on algorithms for non-axisymmetric flows.

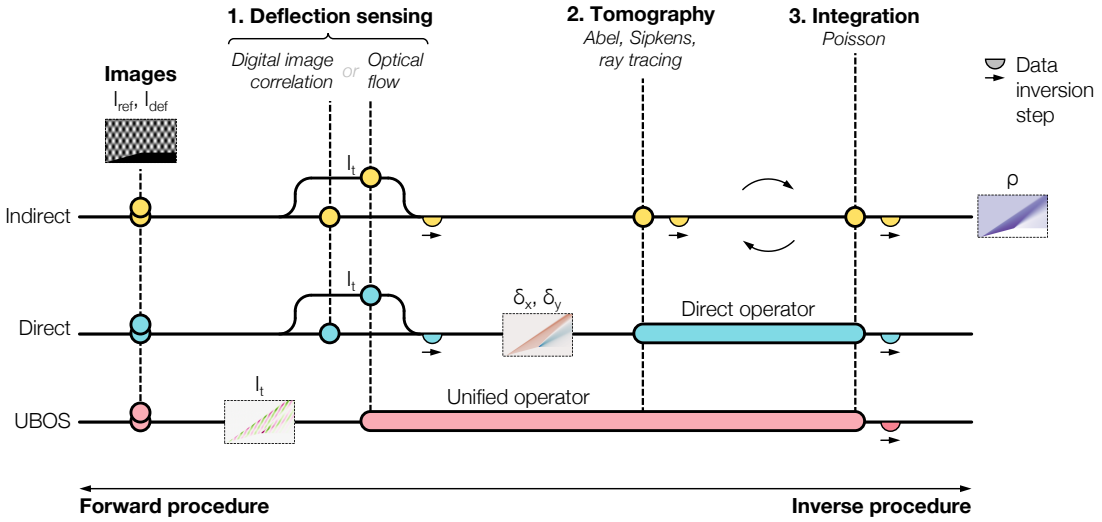

Fig. 7 Graphical overview of quantitative BOS workflow. Adapted from [62] with permission of the authors.

Deflection sensing is discussed in detail in Sec. III, while a pedagogical overview of the Poisson step, though less commonly used in practice, is provided by Rajendran et al. [16]. Tomographic reconstruction for BOS, however, warrants further exposition. These algorithms are generally classified into three categories: analytical, algebraic, and neural. For a comprehensive taxonomy of reconstruction methods and overview of recent developments, refer to Grauer et al. [63]. Each category is outlined below.

1. Analytical Reconstruction Algorithms

Analytical algorithms, such as filtered back projection (FBP), express the inverse measurement model as a closed-form function of the projection data [64]. These algorithms are foundational to many commercial tomography scanners, including those used in medical imaging and non-destructive testing. However, analytical methods typically require a dense set of projection data for accurate reconstruction: often 360 to 1600 views in a standard medical scanner, for instance. This amount of data is untenable in BOS, particularly in the case of time-resolved 3D imaging. A comparatively small number of views (fewer than 30) is used, resulting in a "limited-data" reconstruction problem. Although some early demonstrations of BOS tomography utilized FBP methods [43], analytical algorithms generally perform poorly under these constraints and are seldom applied in contemporary BOS applications.

2. Algebraic Reconstruction Algorithms

Algebraic algorithms are the most widely used methods for BOS tomography. These techniques discretize the field of interest and the measurement equations, yielding a linear system. For example, the density field can be discretized using a voxel basis,

$$\rho(\underline{x}) \approx \sum_j \rho_j \, \varphi_j(\underline{x}) \,, \tag{26}$$

where the basis function φ_j equals unity inside the j^{th} voxel and zero elsewhere and ρ_j is the corresponding coefficient. While voxels are the most common choice, radial basis functions have also been used [65]. While voxels are the most common basis, radial basis functions have also been employed [65]. Line integrals over the field are expressed as matrix operations. Starting with the path integral over a generic scalar field, g, the relationship to the BOS model can then be established. For the i^{th} projection of g, we have

$$b_i = \int_{i^{\text{th}}\text{ ray}} \rho \, \mathrm{d}s \approx \sum_j \int_{i^{\text{th}}\text{ ray}} \rho_j \, \varphi_j \, \mathrm{d}s = \sum_j \rho_j \underbrace{\int_{i^{\text{th}}\text{ ray}} \varphi_j \, \mathrm{d}s}_{S_{i,j}}, \tag{27}$$

where ρ_j is constant within each voxel and $S_{i,j} \equiv \partial b_i / \partial \rho_j$ is the sensitivity of the i^{th} projection to the j^{th} coefficient. Collecting b_i and ρ_j into the vectors $\underline{b}$ and $\underline{\rho}$, respectively, and forming a sensitivity matrix $\mathbf{S}$, with elements for each projection and basis function, the full set of deflection data can be approximated with a matrix equation,

$$\mathbf{S}\underline{\rho} = \underline{b}. \tag{28}$$

Matrix inversion methods can be used to compute $\underline{\rho}$ from $\underline{b}$, for example, via a least-squares approach: $\hat{\underline{\rho}} = (\mathbf{S}^\top \mathbf{S})^{-1} \mathbf{S}^\top \underline{b}$. However, two key challenges arise: (1) In limited-data tomography, the column rank of $\mathbf{S}$ is less than the size of $\underline{\rho}$, leading to an infinite set of solutions, most of which are non-physical [66, 67]; and (2) To achieve a unique and physically plausible solution, additional information, or *regularization*, is required.

It is important to distinguish between the supplemental information used to regularize Eq. (28) and the optimization technique (or similar) used to solve the augmented system of equations. Ideally, an explicit regularization method with a well-understood effect on the solution should be employed, ensuring that the inductive biases inherent to the chosen solver do not affect the final result. Explicit regularization methods frequently involve adding an extra matrix equation. For example, second-order Tikhonov regularization results in a convex optimization problem,

$$\hat{\underline{\rho}} = \arg\min_{\underline{\rho}} \, \|\mathbf{S}\underline{\rho} - \underline{b}\|_2^2 + \gamma^2 \left\|\nabla^2 \underline{\rho}\right\|_2^2 \,, \tag{29}$$

where ∇^2 is the discrete Laplacian and γ is the regularization parameter. At intermediate values of γ, this method produces spatially-smooth solutions that approximately satisfy $\underline{b}$. Although edge-preserving methods like total variation (TV) [58] or total global variation [68] can improve reconstruction accuracy, their implementation is significantly more complex than Tikhonov regularization, which can be performed using built-in functions in MATLAB. For an overview of reconstruction algorithms for limited-data tomography problems based on Eq. (28), see Ref. [63].

The second challenge with Eq. (28) stems from the fact that the integrand in BOS models involves the gradient of ρ (or n) rather than ρ itself. As a result, the model is more complex than the integral over ρ shown in Eq. (27). To address this complication, multiple reconstruction strategies have been developed. One approach involves performing three separate scalar tomography problems to reconstruct each component of $\nabla\rho$ individually. These reconstructions are then

post-processed by solving a Poisson equation to obtain ρ. This method was demonstrated by Atcheson et al. [53] in their pioneering work on 3D BOS tomography. Nicolas et al. [57] then proposed a direct method that avoids the need for a Poisson equation. Their approach introduces an augmented matrix system,

$$\begin{bmatrix} \mathbf{S}\nabla_x \\ \mathbf{S}\nabla_y \\ \mathbf{S}\nabla_z \end{bmatrix} \underline{\rho} = \begin{bmatrix} \underline{b}_x \\ \underline{b}_y \\ \underline{b}_z \end{bmatrix}, \tag{30}$$

Here, ∇_β represents the discrete gradient operator in the β-direction, with $\beta \in x, y, z$, and $\underline{b}_\beta$ contains the β-direction turning angles (or deflections). When deflections are used, they must be projected onto the plane of the corresponding background pattern [58]. In contrast, using turning angles, as demonstrated by Nicolas et al.[57], eliminates the need for projection, with only two components of $\underline{\varepsilon}$ per pixel. In the earlier work of Goldhahn & Seume [43], a proto-direct reconstruction was performed in the Fourier domain, where differentiation corresponds to multiplication by a wavenumber (see the discussion in Ref. [61]). Later, Grauer & Steinberg [35] extended the direct approach from Nicolas et al. [57] by incorporating Eq. (30) into the linear optical flow equation. This integration results in a matrix system that directly links the density or refractive index field to the image data, thereby eliminating the deflection-sensing step and reducing associated errors. These methods are versatile tools for reconstructing 3D BOS data. Analogous approaches for axisymmetric BOS reconstructions have been developed, as highlighted by Xiong, Sipkens, et al. [60, 61].

3. Neural Reconstruction Algorithms

It is worth noting the significant advancements in applying machine learning, particularly deep neural networks, to tomographic imaging [69–71], including BOS tomography [72]. Many of these neural algorithms operate within a supervised learning framework, where a neural network is trained to map projection data to the desired quantities, such as taking $\underline{b}$ as input and outputting $\underline{\rho}$. Training usually involves $(\underline{\rho}, \underline{b})$ pairs, with $\underline{\rho}$ generated from one or more representative simulations and $\underline{b}$ computed using the forward model. These networks often produce accurate reconstructions of density or refractive index fields for data resembling the training set. Moreover, they offer remarkably fast reconstruction times, often on the order of seconds or less. Challenges arise when reconstructing "out-of-sample" data: flows that differ significantly from those in the training set. This limitation reduces the utility of supervised learning algorithms, as their performance relies heavily on the fidelity of simulation tools used to generate training data and the comprehensiveness of the training set. As a result, these algorithms may fail to accurately recover flow structures that are poorly modeled by computational fluid dynamics (CFD). Conversely, if a flow can already be reliably simulated with CFD, the additional value of BOS tomography becomes unclear. To address these issues, researchers have explored specialized neural network architectures that incorporate inductive biases to improve generalization to out-of-sample data. The generalizability of such techniques remains an open question.

An emerging alternative approach to reconstruction is the neural-implicit reconstruction technique (NIRT), which originated in X-ray tomography [73–76] and has recently been applied to BOS [77–79]. This method employs a neural network to map spatio-temporal input coordinates $(\underline{x}, t)$, to the scalar or vector fields of interest at the position $\underline{x}$ and time t. This is often called a "coordinate neural network." For instance, in BOS tomography, the network maps $(\underline{x}, t) \mapsto \rho$. NIRT can also be utilized for data assimilation, as discussed in Sec. V.D. The network is trained to reconstruct fields that satisfy both the measurement data and any supplemental information about the flow. Notably, a separate network is trained for each reconstruction, with the network parameters optimized to minimize an objective loss function,

$$\mathcal{J} = \mathcal{J}_\mathrm{D} + \gamma \mathcal{J}_\mathrm{R}, \tag{31}$$

where $\mathcal{J}_\mathrm{D}$ is a data fidelity term and $\mathcal{J}_\mathrm{R}$ is a regularization term. A typical data loss is

$$\mathcal{J}_\mathrm{D} = \sum_i \sum_\beta \left\| d_{\beta,i} - \frac{\psi M z_\mathrm{B} G}{n_0} \int_{i^\mathrm{th}\ \mathrm{ray}} \nabla\rho \, \mathrm{d}s \right\|_2^2, \tag{32}$$

where i loops over all the pixels of the imaging system, β loops over each component of the data, and the integral is approximated using Monte Carlo sampling. Importantly, this formulation can be replaced with a unified model based on the non-linear optical flow equation and cone-beam geometry [77], enabling the reconstruction algorithm to account for large deflections and finite depth-of-field effects. When the network is trained to minimize $\mathcal{J}_\mathrm{D}$, projections of the density field represented by the network match the experimental data.

Coordinate neural networks based on a simple feedforward multilayer perceptron exhibit a low-frequency spectral bias when optimized by stochastic gradient descent, which tends to smooth out flow features. While some researchers exploit this bias as a form of implicit regularization, the network's capacity to represent broadband spectral content, e.g. in turbulent flows, can be enhanced by introducing a Fourier encoding layer between the input and the first hidden layer [80]. However, incorporating this encoding also allows the network to recover spurious features, necessitating the use of an explicit regularization term, $\mathcal{J}_\mathrm{R}$. This penalty can be based on a continuous formulation of a conventional regularization term, such as a Tikhonov or TV penalty, or it can derive from the governing equations of the target flow, as discussed later in Sec. V.D. NIRT algorithms offer several key advantages: (1) they provide significant data compression, (2) they readily accommodate advanced measurement models, such as those involving non-linear ray tracing and image warping, and (3) they enable a space–time parametrization, allowing for temporal sparsity regularization and comprehensive data assimilation. These features make NIRT algorithms a promising tool, and their adoption in BOS tomography is expected to grow in the future.

C. Developments in BOS Tomography

Tomographic BOS has become a key tool for capturing unsteady structures in variable-density flows. This section does not provide a comprehensive review but highlights considerations for instrumentation and offers selected examples that illustrate recent advances in BOS tomography. The discussion focuses on non-axisymmetric flows, where multi-view imaging is needed for quantitative 3D reconstructions. While axisymmetric setups often use simpler techniques like Abel inversion, broader discussions of reconstruction methods for axisymmetric BOS can be found in Refs. [10, 60, 61].

1. Instrumentation and Imaging

Quantitative reconstruction of a non-axisymmetric 3D field via BOS requires multiple viewpoints. Synchronous imaging is essential for instantaneous measurements, but mean-field reconstructions can be performed using asynchronous BOS data. Synchronous data is either recorded with a network of cameras or one or two cameras coupled to a series of fiber-based endoscopes [81]. In contrast, asynchronous data can be recorded from multiple perspectives by rotating the flow or test article (rotisserie-style) or translating the camera around the domain between acquisitions. Reconstruction errors theoretically decay exponentially with the number of views, making it advantageous to maximize the view count [63]. However, practical limits arise from factors like imprecise camera calibrations and noise, including both sensor noise and spatio-temporal oscillations in the background intensity. Typical BOS systems employ six to 30 views, with most falling in the range of eight-to-15. Cameras are often distributed around a semi-circle, ideally with an equi-angular spacing of $\pi/(N_\mathrm{views}+1)$, where N_views is the number of vantage points. An example of this layout is shown in Fig. 8, where 23 cameras are distributed around a 165° arc [35]. For setups with many cameras, shared BOS backgrounds may be necessary, requiring careful estimation of background orientation and projected deflections.

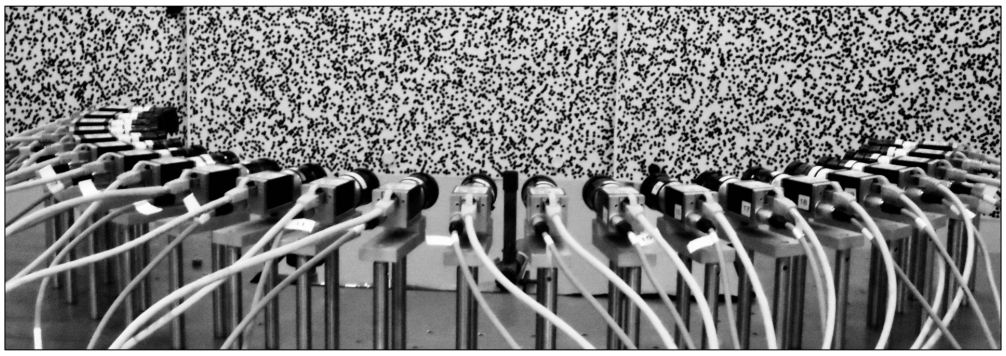

Fig. 8 Sample 23-camera BOS tomography setup for combustion imaging. Adapted with permission from Ref. [58].

Camera calibration is a critical aspect of BOS tomography. Accurate calibration maps each pixel to a line of sight through the domain and to a terminal position on the background. Calibration typically involves imaging a target marked with well-defined control-points, while translating or rotating the target within the field of view. These images are used to generate pairs of world and sensor points, $(\underline{x}, \underline{u})$, for estimating camera model parameters. Unlike planar or stereo PIV setups, BOS tomography requires explicit camera models to address the challenge of limited shared field of view

among all cameras. Cameras must be modeled within a shared global coordinate system, and fiduciary markers on the backgrounds are helpful for estimating their poses during calibration. For further details on workflows and inversion of camera models, see Grauer et al. [63], which discusses near-identical procedures for emission tomography.

Lighting and synchronization are equally critical. External triggering of cameras and illumination via a digital delay/pulse generator ensures consistent image capture across views. Powerful illumination is required, especially for flows with natural luminosity (e.g. flames or detonations), and care must be taken to avoid quasi-shadowgraph effects caused by refraction of light directed towards the background, especially when using point-like illumination. To freeze flow flow structures in each image acquisition, the duration of illumination should be minimized. Data management is another essential consideration: BOS tomography experiments can produce gigabytes to terabytes of data per run, necessitating reliable streaming of images to onboard memory or external storage. Achieving the desired frame rate often requires a custom hardware solution.

2. Contemporary Examples

Recent demonstrations of BOS tomography have spanned diverse applications, including external aerodynamics, propulsion-related flows, atmospheric combustion, and jets. The following studies showcase the technique's adaptability to complex flow environments and its utility for quantitative 3D and 4D measurements.

High-speed aerodynamic flows have been a focus of national aerospace agencies such as NASA, ONERA (France), and JAXA (Japan). Bathel et al. [82] outlined preparations for BOS tomography in NASA's 31-Inch Mach 10 Air Wind Tunnel, conducting tabletop tests with candle plumes and heated air jets to refine methods for camera calibration and background pattern design. Similarly, Takahashi et al. [83] performed BOS tomography in a blowdown wind tunnel at JAXA's Chofu Aerospace Center, reconstructing the mean 3D shock structure around a 25%-scale sounding rocket model. Using a single-camera telecentric BOS setup and a rotisserie-mounted model, they captured detailed visualizations of oblique shock structures (see Fig. 9a). Tangentially, in propulsion-related research, Gupta et al. [84] used BOS tomography to investigate the exhaust of a rotating detonation engine (RDE): a challenging flow environment with steep density gradients and rapid temporal dynamics. Their study revealed the intricate structure of detonation-driven flows, providing critical insights into exhaust behavior and its implications for engine performance; a sample cross section of density in the exhaust from their study is shown in Fig. 9b.

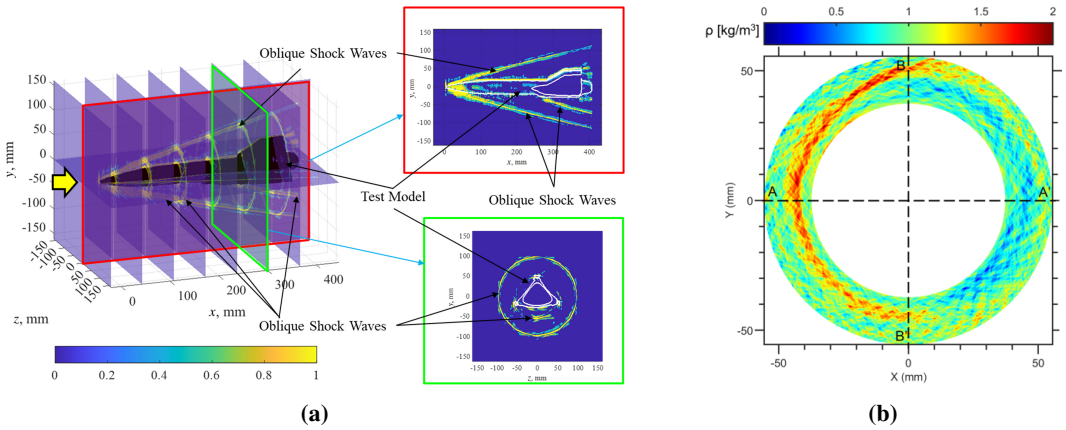

Fig. 9 Tomographic BOS reconstructions showing (a) the shock structure around a 25%-scale sounding rocket model and (b) the exhaust of a RDE. Adapted with permission from Ref. [82, 84].

BOS tomography has also been applied to atmospheric flames, an area of growing interest due to its potential for capturing quantitative 3D temperature and density fields in flames and detonations [85]. These measurements hold promise for validating combustion models and advancing our understanding of flame dynamics, including coherent temperature structures and flame-front propagation speeds as a function of surface area. However, significant challenges remain in correlating the refractive index field to parameters like temperature or density. Composition gradients in reacting flows introduce ambiguities in the relationship between n, ρ, and T, complicating direct interpretation. Early work by Grauer et al. [58] pioneered the use of BOS tomography for combustion, paving the way for multi-modal approaches that integrate BOS with techniques such as chemiluminescence tomography and tomographic emission thermometry. For example, Martins et al. [86] used joint BOS–flame radical–temperature reconstructions to investigate

the relationships between reacting zones and thermal structures under various operating conditions in turbulent combustion and nanoparticle synthesis. Further advancements are needed to enhance spatio-temporal resolution and resolve ambiguities when estimating the thermochemical state from BOS data.

Jet flows represent another prominent application of BOS tomography, with several examples of multi-modal experiments used to uncover complex flow phenomena. Nicolas et al. [87] and Akamine et al. [88] combined BOS with complementary techniques, such as microphone arrays and stereo PIV, to study heated air jets. Akamine et al. [88] explored the relationship between coherent jet structures and acoustic noise production, while Nicolas et al. [87] visualized mixing layers driven by Kelvin–Helmholtz instabilities at ONERA. Figure 10 presents representative reconstructions from these efforts. In a related ONERA study, Lanzillotta et al. [89] examined the modal structure of a screeching jet. Another jet study by Amjad et al.[90] evaluated reconstruction algorithms for heated turbulent jets using synthetic BOS data, identifying challenges associated with blurring and angular sparsity in the data; they complemented their findings with experimental reconstructions and direct numerical simulations.[§] Collectively, these studies highlight the adaptability of BOS tomography for jet flows and the growing reliance on multi-modal approaches for deeper analysis of flow phenomena.

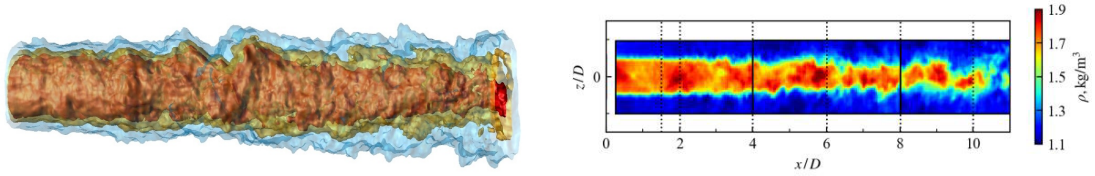

(a) **(b)**

Fig. 10 3D density field reconstructions of axisymmetric jets: (a) isosurfaces of ρ in a heated jet and (b) cross-section of ρ in a perfectly expanded Mach 1.8 jet. Adapted with permission from Ref. [87, 88].

D. Data Assimilation

Data assimilation is a promising alternative to traditional BOS processing techniques. Experimental observations are combined with numerical models to estimate a system's state, often enabling predictions of its future evolution [91]. In fluid dynamics, there is growing interest in leveraging data assimilation to enhance experimental analyses by integrating measurements with a numerical model, such as one based on the continuity and Navier–Stokes equations. This approach aims to achieve "inverse CFD," wherein CFD-quality reconstructions of all the flow variables (density, velocity, pressure, etc.) are computed while adhering to the governing equations as constraints.[¶] Data assimilation can seamlessly incorporate multi-modal, multi-fidelity measurements, allowing BOS data to be integrated with complementary sensor outputs, such as infrared thermography and pressure-sensitive paint [92] or stereo PIV [87]. By enabling sensor fusion, this methodology opens up new possibilities for observing and analyzing complex flow behaviors that are otherwise challenging to simulate without experimental constraints, offering unparalleled insight into fluid dynamics.

Numerous data assimilation techniques have been applied to fluid dynamics, including Kalman filter methods, state observers, adjoint–variational frameworks, and hybrid simulations. Only a few of these methods have been applied to BOS, however. For example, at ONERA, Ali et al. [93] employed a Kalman filter to sequentially update turbulence model parameters and match synthetic BOS measurements by repeatedly solving the Reynolds-averaged Navier–Stokes (RANS) equations. Hybrid simulations represent another strategy, where one or more fields or parameters are constrained by experimental data. For instance, Vinnichenko et al. [94] performed a hybrid simulation of natural convection by incorporating BOS-derived temperature fields to estimate buoyancy forces. In this approach, the experimentally measured temperature field was directly utilized by the solver, bypassing the need to solve for temperature.

A closely related class of data assimilation algorithms is physics-informed neural networks (PINNs), which integrate data and governing equations through a coordinate neural network [95]. Similar to NIRT, PINNs represent flow field variables with a coordinate neural network. However, instead of using a single output, PINNs output all the dynamically relevant variables, and instead of minimizing a regularization term like $\mathcal{J}_R$ in Eq. (31), PINNs enforce

[§]Molnar et al. [77] recently introduced a NIRT algorithm that accounts for optical blur by modeling the cameras' collection geometry, addressing key limitations in jet imaging.

[¶]This stands in contrast to conventional CFD simulations, which correspond to boundary-value problems. Hence "inverse CFD" as opposed to the usual forward approach.

physical constraints by minimizing a loss term, $\mathcal{J}_P$, that includes volume-integrated residuals of the governing equations. This approach leverages automatic differentiation to rapidly compute exact partial derivatives of the network, enabling accurate and computationally efficient evaluation of $\mathcal{J}_P$. By simultaneously minimizing the data fidelity $\mathcal{J}_D$ and physical consistency $\mathcal{J}_P$, PINNs produce reconstructions that adhere to both experimental data and fundamental physical laws. Key advantages of PINNs include their data compression capabilities, particularly for 3D and 4D flows, scalability, robustness, and ease of implementation, making them a compelling option for flow reconstruction.

PINNs were first applied to BOS data as a post-processing tool by Cai et al. [96], who used a six-camera BOS tomography setup to study natural convection above an espresso cup. The reconstructed temperature field was fed into a PINN, which utilized the Navier–Stokes equations with a Boussinesq approximation, to estimate velocity and pressure fields. PIV measurements were performed for validation, showing good agreement. While Cai et al.'s approach processed BOS data after the tomographic reconstruction step (which is subject to errors), Molnar et al.[97] integrated BOS data directly into the assimilation procedure. They applied their method to classical cone–shock data from Venkatakrishnan [48, 49] and synthetic test cases, reconstructing steady density, velocity, and pressure fields by solving the compressible Euler equations with an equation of state. Figure X shows sample reconstructions from this study, validated against numerical data and the cone shock tables from Sims [98].

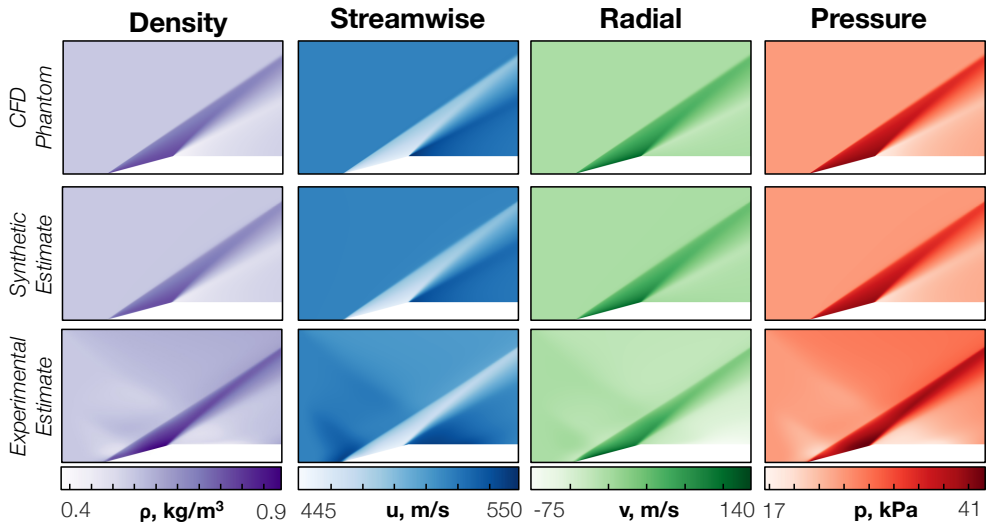

Fig. 11 Numerical phantom, synthetic reconstruction, and experimental reconstruction of a cone–cylinder shock using BOS data assimilation. Adapted with permission from Ref. [97].

Subsequent work extended these methods to turbulent flows. The groups of Grauer [99] and Weiss [100] employed BOS data in RANS-based data assimilation for underexpanded jets and shock wave–boundary layer interactions, respectively. BOS is particularly well suited to this approach since the density field is unchanged by a Favre average, whereas other experimental signals cannot be directly linked to the output of a compressible RANS model. Future research is expected to expand BOS data assimilation to time-resolved compressible flows, enabling more accurate measurements of density and the simultaneous inference of velocity and pressure fields.

E. Event-Based BOS

A recent innovation that deserves a brief discussion is Event-based BOS (EBOS). EBOS is a technique that takes advantage of event-based cameras to measure the density fluctuations caused by schlieren. Event-based cameras, also known as dynamic vision sensors, are a new type of camera that, unlike conventional image-based cameras, asynchronously image only pixel locations where the brightness changes by more than a certain value [101, 102]. These cameras offer potential advantages over conventional image-based cameras, such as high dynamic range, temporal resolution and data efficiency [103]. Compared to image-based cameras, event-based cameras can achieve very low data redundancy, which enables low power consumption, high dynamic range, and microsecond time resolution and latency, and therefore offer great potential for high-frame-rate BOS applications [102]. Over the past decade, researchers have attempted to use event-based cameras for flow visualization in other contexts, including particle image and particle

tracking velocimetry, which share similarities with BOS [104–107]. Shiba et al. [103] presented the first theoretical analysis combining event-based image data and schlieren under continuous illumination, and visualized air convection using event data and conventional images. A key difference between image-based BOS and event-based BOS is that event-based cameras only capture temporal changes in the scene, while the former measure the displacement between a reference image and the current image [103]. This enables the observation of air convection at high speed and under difficult lighting conditions. Because of their high data efficiency, EBOS systems can continuously record the flow over an extended period of time at frame rates in the kHz range without being limited by the camera memory. In addition, EBOS systems do not require high-power light sources, which is due to the high sensitivity of the event-based sensor. The laser used by Lyu et al. [102] has a power of only 150 mW, which is two orders of magnitude lower than the power of light sources used in similar experiments, for instance. Finally, EBOS systems are significantly less expensive than image-based BOS systems with high frame rates.

In order to reconstruct an image, a time window must be defined within which the events are accumulated. For pulsed illumination, the time window corresponds to the interval between two light pulses [101], and each reconstructed image represents the flow field at the time of the light pulse. For continuous illumination, the time window is often determined empirically [101]. The event data over a period of time is simply overlaid to reconstruct the images. In some EBOS systems, event data is combined with image data from an image-based camera to improve image reconstruction. The image data provides additional spatial information that can increase the accuracy and detail of the reconstructed images [102]. The consideration of factors such as readout latency, noise and the possible combination with image data is crucial for the generation of accurate and meaningful images of the flow field. This allows EBOS to view flow phenomena on different time scales simultaneously.

VI. Unique Applications in Challenging Environments

The BOS method is particularly suited to applications in environments where traditional optics are not large enough to image the event or would not survive testing. A few important examples are listed here. While this list is by no means comprehensive, it is intended to give the reader a sense of the remarkable range of applicability and flexibility of the BOS technique, which continues to be expanded.

A. High-Speed Imaging in Large-Scale Ground Test Facilities

In this section, we restrict the discussion to BOS measurements that are both acquired at framing rates above 1 kHz and capture the time-correlated evolution of flow structures between sequential frames. In these measurements, a high-speed camera is required that is capable of achieving high framing rates with a spatial resolution sufficient to capture the region-of-interest/field-of-view at a magnification that resolves both the background pattern features and flow structures of interest. Currently, a number of camera options are available from many different manufacturers with a wide range of resolutions, framing rates, and bit depths, including ultra high-speed variants (e.g. Photron, Phantom, iX Cameras, Shimadzu, Specialised Imaging, etc.), that can acquire image sequences at resolutions around 1 Megapixel at framing rates in excess of 20 kHz, and at reduced resolutions at framing rates in excess of 1 MHz.

As will be discussed in the following section, BOS measurements have been used to visualize the propagation of shock waves over a large field-of-view resulting from explosions at framing rates of 3–15 kHz [108–110]. These outdoor measurements were conducted using ambient daylight with sufficient intensity to image natural backgrounds with enough contrasting features to constitute a BOS background, similar to that shown in Fig. 16. However, in ground test facilities requiring high-speed BOS measurements, continuous and pulsed high-intensity light sources are used to illuminate BOS background patterns so that the signal from contrasting pattern features provide displacement measurements with high accuracy and precision. At moderate framing rates, a simple and straightforward approach for high-speed BOS imaging is to use forward illumination on a diffuse surface such as paper with a printed pattern. This method was used by Mizukaki et al. [111] with a photographic strobe light used to illuminate a patterned paper background to capture BOS data at 10 kHz of vortex rings generated by a shock tube. Note that the light source used must be sufficiently large (e.g. by placing a diffuser just beyond the source) so that it does not produce a competing shadowgraph signal. Further, the light source must be carefully placed to minimize shadows from wind tunnel models or other occluding objects, which can interfere with the measurement.

As the need to increase framing rates reduces the maximum achievable exposure, higher intensity light sources and more efficient methods of light collection are needed so that the background pattern signal can be maintained at a satisfactory level. Stasicki et al. [112, 113] showed that LEDs could be used to visualize high-speed fluid dynamic phenomena as their output intensity could be dramatically increased by driving them with pulsed currents higher

than those used for continuous operation. Willert et al. [114] later showed that these devices could be driven with currents up to 200 A with pulses as short as 100 ns, in some instances at significant duty cycles ($\geq$ 25%) for short bursts. Several LED-based illumination options, such as those described by Stasicki et al. [115] and others that are available commercially, now exist for high-speed BOS applications and avoid known problems with eye safety and speckle associated with coherent laser light sources. When even higher intensity sources are required for higher speed applications, laser light sources can be used. Commercial options (e.g. Cavilux HF and Smart, Specialised Imaging SI-LUX, etc.) can produce high-intensity, low-coherence laser-diode-based illumination that is speckle-free and can be pulsed at rates up to 10 MHz. Cost-effective, laser-diode-based sources with limited speckle can also be constructed from commercially-available components for pulsed BOS illumination, with some examples described in Refs. [116, 117]. Light from pulsed laser sources with a high degree of coherence have also been used for high-speed BOS measurements at framing rates of 20 kHz [118], where the laser speckle formed on the background serves as the BOS pattern with the sizing of the speckled features being a function of the laser wavelength and $f_\#$ of the lens projecting the light [119].

To more efficiently capture light in high-speed BOS systems, researchers [120–122] have used back-illuminated transparent patterns that couple light from the background pattern directly into the high-speed camera lens, thereby enabling framing rates much higher than typically possible with forward-illuminated backgrounds. Some limitations of this approach include requiring optical access on opposing sides of the measurement region, constraints on the size of the measurement region to one less than that of the optical access on the side with the background pattern, and that it may require additional optics (such as a Fresnel lens) to be placed behind the transparent background to focus the light into the camera lens on the opposing side. To avoid these limitations, Heineck et al. [123] showed that forward-illuminated retroreflective sheeting could be used to provide high contrast patterned backgrounds on which BOS measurements could be acquired with high light collection efficiency. Retroreflective sheeting can be purchased in large sizes (e.g. 24-inch by 50-yard rolls), with an adhesive backing that allows it to be mounted to the walls of ground test facilities, and is designed to return light most strongly along its axis of incidence. Since the reflected intensity for these materials is greatest when the imaging axis and lighting axis are co-linear and quickly diminishes as they are angled relative to one another (functionally described by the bidirectional reflectance distribution function, or BDRF [124, 125]), the light sources used to illuminate them are often placed near to the imaging camera, such as with the use of ring lighting, or made to be co-linear with a beamsplitter. Use of co-linear illumination also minimizes the presence of shadows cast by wind tunnel models or other occluding objects. As noted in Ref. [126], care must be taken to select a retroreflective sheeting that will withstand the environmental conditions within the test facility. For larger-scale ground test facilities with challenging environmental conditions, retroreflective sheeting with embedded microspheres, such as 3M's Scotchlite 7610 material, have fared well [82, 126]. By laminating this thin retroreflective sheeting to vinyl adhesive film, Weisberger et al. [127] found that application of retroreflective sheeting in large-scale ground test facilities could be quickly applied and removed from test section walls without degradation of the material. To ensure that patterns applied to these retroreflective materials were able to withstand the harsh conditions during test campaigns, a method of splattering latex-based paint with an air sprayer was developed at NASA Ames Research Center that allowed for reliable control of pattern size and distribution [123]. These researchers were later able to use screen printing methods for even more precise control of pattern size and distribution [127].

To demonstrate the effectiveness of the different illumination methods and types of background patterns, a set of high-speed BOS measurements were performed. For all measurements, a high-speed camera operating at a framing rate of 100 kHz was used to capture the BOS images using an adjustable zoom lens with f = 85 mm and the $f_\#$ set to 11. For these measurements, the patterned background was placed approximately 1 m from the lens and the density disturbance positioned 330 mm from the pattern background. Three different patterned background types were considered: one of white paper, one a transparency, and one of retroreflective sheeting (3M Scotchlite 7610). A random dot pattern created with LaVision's Random Pattern Generator software was printed on each material, where the dots had a diameter of 500 µm and a minimum spacing of 250 µm. Light at 640 nm from a Cavilux HF laser was highly expanded and then passed through a diffuser to uniformly illuminate the backgrounds. For the retroreflective background, the same laser source with the diffuser was coupled into an imaging optical isolator consisting of a polarizing beamsplitter and quarter-wave plate to provide illumination that was colinear with the imaging axis. For the transparency background setup, the laser source was placed behind a ground glass diffuser and was followed by a Fresnel lens to provide a uniform illumination intensity. The transparency was positioned approximately 130 mm in front of the Fresnel lens to blur its surface features in the final BOS images.

As mentioned previously, the size and placement of the light source must be considered when using forward illumination. Figure 12 shows BOS images obtained using forward illumination of the paper background. In these images, the placement of the light source results in a shadow being cast onto the background by the nozzle of the

heat gun, eliminating the possibility for capturing data over the lower half of the nozzle. By removing the diffuser, a shadowgraph signal is formed on the background pattern as shown in the inset in Fig. 12a, which may interfere with the BOS measurement. When the diffuser is returned to the setup, the shadowgraph artifacts are effectively removed and the edges of the shadow cast by the heat gun are softened, as shown in Fig. 12b.

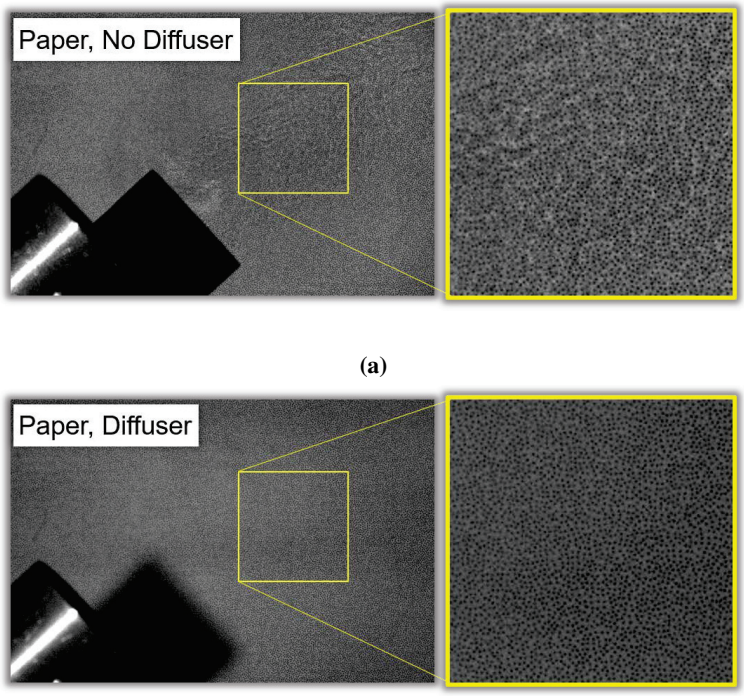

Fig. 12 Forward illumination of a patterned paper background (a) without and (b) with a diffuser to increase the effective light source size.

Figure 13 shows both single-shot data images (top images) and displacement magnitude BOS measurements (bottom images) obtained with the different high-speed BOS illumination methods. For these measurements, the laser pulse width from the Cavilux HF light source was limited to less than, or equal to, 190 ns (a constraint of the laser hardware) so that a framing rate of 100 kHz could be maintained. This pulse width was used for the paper background measurements shown in Fig. 13a. For the transparency background measurements shown in Fig. 13b, a pulse width of 150 ns provided sufficient illumination of the pattern. For the retroreflective background measurements shown in Fig. 13c, the Cavilux HF minimum pulse width of 30 ns was used, providing a pattern contrast similar to, or even slightly better than, that obtained with the transparency background. The displayed intensity range for the single-shot data images shown in the top row of Fig. 13 is kept constant to compare signals between the different methods. Similarly, the displacement magnitude color scale for the BOS measurements is kept constant to allow for their comparison. LaVision's 2D BOS software was used to compute the BOS displacement magnitudes with the same processing settings used for each high-speed image sequence. In the single-shot data images, the light collection efficiency of the paper using the forward illumination method is clearly less than that of the transparency and retroreflective backgrounds, as the pattern contrast is noticeably lower than that of the other methods, even when using the longest laser pulse width. Additionally, a significant amount of noise away from the heat gun flow can be observed. The transparency background and back-illumination method significantly improved the contrast while using a lower laser pulse width and resulted in an observed reduction in noise away from the heat gun flow when compared to the paper background. The retroreflective background and corresponding forward illumination method had excellent light collection efficiency, producing data images with good contrast even with the lowest laser pulse width. Further, noise away from the heat gun flow is far lower than that of the other two methods. Finally, by using forward illumination that is colinear with the viewing axis of the camera, unwanted shadows cast by the heat gun nozzle in Fig. 13a are eliminated.

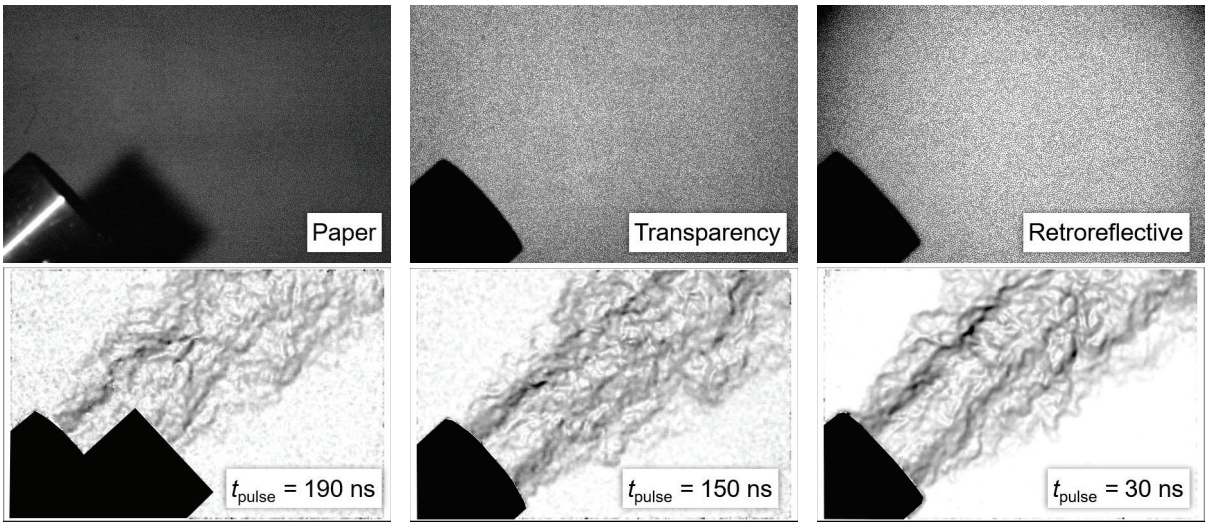

Fig. 13 High-speed BOS displacement magnitude measurements obtained at a framing rate of 100 kHz with the (a) paper background, (b) transparency background, and (c) retroreflective background.

There have been several recent technologies developed that lend themselves to high-speed BOS measurements in large scale test facilities. One challenge with BOS measurements in these facilities is the presence of vibration during facility operation that can result in misalignment between the reference pattern acquired without flow and the deflected images acquired with flow on. Typically, a shift correction is applied to deflected images to align them to the reference image by selecting small regions in the deflected images without distortion of the background pattern and using a cross-correlation (or similar method) to translate the image [27]. Raffel et al. [31] proposed a reference-free (i.e. no requirement for a separate flow-off reference image to be acquired) BOS method in which the projection of a pattern (either a standard randomized dot pattern or laser speckle) is translated over the background plane and a high-speed camera used to capture the pattern in motion. An analysis is then perform between sequential images to obtain a displacement map. Weisberger et al. [128] also developed a reference-free method that co-linearly projected a fixed pattern onto the background and compared these to the original pattern imaged within the instrument.

Another challenge with high-speed BOS measurements in large-scale ground test facilities is the cost associated with high-speed cameras, as well as their size when used in space-restricted areas. As discussed in Sec. V.E, event-based camera technology potentially enables high-speed acquisition with a small footprint and relatively low cost compared to conventional high-speed cameras. Instead of transmitting full images, these devices transmit data associated with changes in intensity. For BOS measurements, refractive index gradients result in distortions in standard patterned backgrounds at various locations throughout the image that are registered as intensity variations. Since a large number of pixel intensity values remain constant between the reference and deflected image, an event-based camera may be utilized to provide a high-speed, compact EBOS measurement capability [101–103].

B. Ballistics and Explosives

BOS visualizations have been regularly observed in ballistic and explosive testing, although not always considered by the term "BOS." Many ballistic and explosive test facilities have historically utilized "zebra boards" as backgrounds erected around test sites to image shock waves as they distort the black-and-white striped interfaces [129–131]. These backgrounds, as shown in Fig. 14, allowed the visualization of the shock wave as discontinuities of the stripes. The structured backgrounds are sensitive only to deflections perpendicular to the stripes, as a traditional schlieren system is sensitive to the distortion perpendicular to the knife edge direction, and thus were frequently aligned at an inclined angle to the expected flow direction. While many today view these backgrounds as present for the purpose of spatial calibrations, their original purpose was to visualize the shock waves [130].

The application of modern BOS imaging and analysis methods in ballistics and explosive testing was slower to be

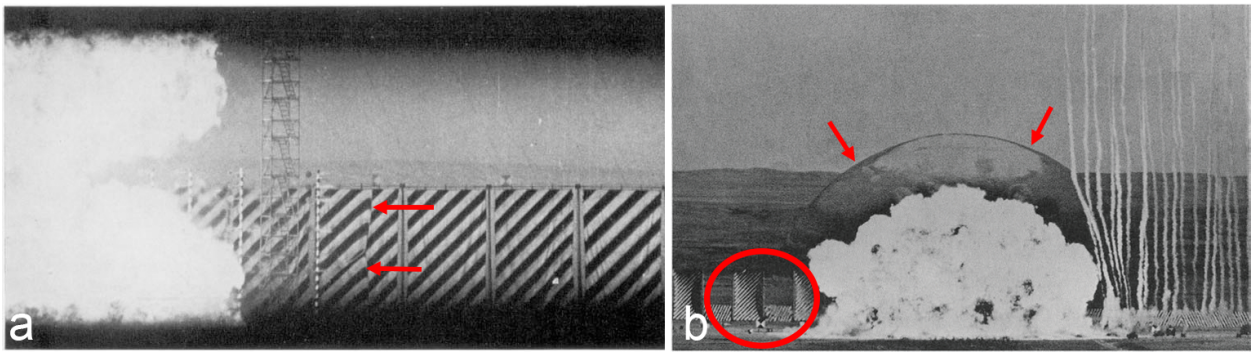

Fig. 14 Background distortions have been observed in explosive testing for many years including the use of (a) "zebra boards" [129] and (b) natural background distortions [130] to image shock wave propagation. The red arrows have been added here to show the shock wave locations and the red circle highlights "zebra boards" used in the large scale test in (b). Note that the rocket smoke trails in image (b) were used to track air velocity motion behind the shock wave, not the shock itself. Images used with permission.

adopted than other fields, even though explosive blast fields regularly produced observable BOS effects as demonstrated in Fig. 14b. One of the first works in the modern BOS era by Sommersel et al. applied BOS imaging to measure shock wave propagation from Composition C-4 (C-4) explosions [108]. The work applied a BOS methodology based on image subtraction and measured shock propagation as a function of time in multiple directions from the blast. Hargather and Settles imaged gunshots and explosions against natural backgrounds and discussed some of the limitations at the time, in particular the lack of high-speed camera resolution and relatively long shutter times needed for outdoor imaging [132]. They also compared BOS images to an image of a gunshot acquired with a large-scale schlieren system and noted the resolution limitations for BOS compared to conventional schlieren. As discussed in Sec. II.C, many of these limitations still persist today, with high-speed cameras still having limited image resolution and outdoor illumination of backgrounds limits shutter speeds.

Many of the applications of BOS for outdoor experiments implement image subtraction processing routines in addition to correlation-based processing. The image subtraction processing typically performs a pixel-by-pixel intensity subtraction between a deflection image and a reference image to identify locations where a pixel intensity value has changed [108, 110, 132]. This works well for explosive testing where the position of the shock wave is one of the primary measurements being made. The pixel-by-pixel subtraction provides better resolution for identifying the shock wave than correlation-based analyses which involves some local averaging. Figure 15 shows a high-speed image of a 1 kg C-4 explosion which is processed relative to a reference image (not shown) with both (b) an image subtraction routine and (c) an optical flow routine. The subtracted image shows a crisp shock wave, but does not provide the quantitative measurement of the background distortion which is provided by the optical flow processing. The subtraction processing can also include many artifacts because it is only identifying locations where light intensity has changed. This is addressed in some works by performing a "sequential subtraction" of several consecutive high-speed video frames to visualize the shock as it moves from one frame to another [133]. This subtraction processing is almost exclusively applied by the blast testing community, but yields high-quality visualization of shock wave locations [110] and fragments produced by explosions [134, 135].

BOS techniques have expanded the quantitative information available from explosive testing. One of the most common measurements in blast testing is tracking the shock wave position versus time, which can be utilized to calculate the blast overpressure. Many researchers have applied BOS to calculate this quantity and compared it to blast correlations or scalings [108, 109, 136]. Hargather demonstrated calculating explosive overpressure from BOS-visualized shock wave propagation compared favorably to pressure gauges for large-scale explosive testing [110]. Venkatakrishnan et al. applied BOS in the laboratory to image small-scale shock waves from detonation tubes and demonstrated the potential to measure density fields in shock waves [137]. Yamamoto et al. applied BOS to underwater shock waves and applied an additional visualization of the Laplacian of the displacement field to approximate a shadowgram [138] Winter and Hargather applied a multiple-camera BOS setup to reconstruct three-dimensional shock wave positions versus time from field explosions [133]. Strebe recently applied BOS with a 9-Megapixel high-resolution, high-speed camera to measure shock wave propagation and density fields, which were utilized to estimate the entire blast pressure profile that in turn

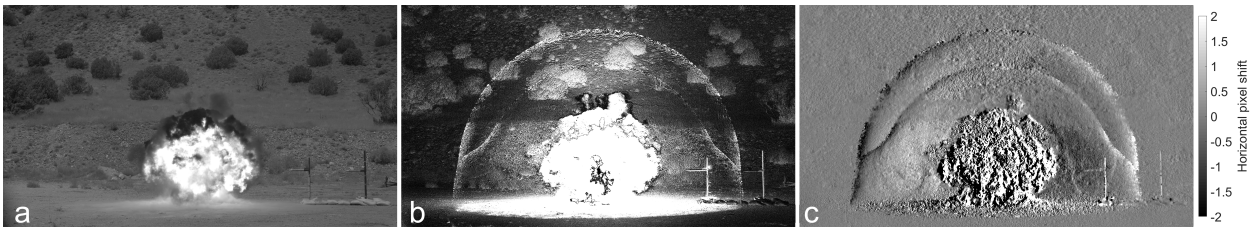

Fig. 15 (a) A high-speed image of a 1 kg C-4 explosion is compared to a pre-test image and processed with (b) pixel intensity subtractions or (c) optical flow algorithms to visualize the shock wave produced. Images used with permission of the authors.

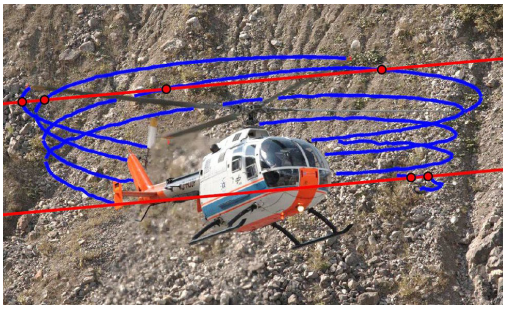

Fig. 16 Multi-camera mapping of helicopter vortices in hover using natural background BOS and epipolar analysis [142]. Image used with permission of the authors.

was compared to direct pressure measurements [139]. The work by Strebe was adapted here to produce Fig. 15.

The evolution of the application of BOS for explosives testing has thus grown from simple position measurements of shock waves to density fields in large-scale explosions. Camera developments continue to enable better temporal and spatial resolutions for these outdoor tests. Explosive studies are particularly challenging because the flows are inherently time-varying, which limits image averaging and smoothing of processing routines which can be used in some of the ground-test and free-flight analyses.

C. Airborne and *In Situ* Imaging With Natural Backgrounds

The first successful effort to deterministically and repeatably obtain a schlieren image of a supersonic aircraft in flight was performed by Weinstein [21]. This generational achievement opened the doors for developing other airborne schlieren methods using digital imaging for aircraft in flight. Subsequently two methods involving BOS have produced higher-fidelity imagery than that of the original Weinstein method. The first is a two-aircraft methodology called Airborne Background Oriented Schlieren (AirBOS), where an observer camera in one aircraft images features on the Earth's surface as the target aircraft flies between [23, 140]. The second, called Background Oriented Schlieren using Celestial Objects (BOSCO), makes use of the solar disk as viewed through solar telescope fitted with an etalon that reveals the visual surface texture of the sun. The imagery is captured using a high-speed digital camera as the aircraft flies through a very small window in the sky to eclipse the sun [141].

BOS imagery of helicopters in flight was pioneered by the DLR Goettingen Department of Helicopters. That history is well described by Bauknecht et al. [140, 142], where helicopter blade tip vortices were imaged from a second helicopter using DSLR cameras. In one major flight experiment, six DSLR cameras with long focal-length lenses were used and the face of a quarry served as the background. Significant effort was put into characterizing the visual texture of various locations in the quarry. Once the best location was established the flight planning and optical set-up was optimized. Hover, forward flight, and banking maneuvers conditions were captured. The subsequent schlieren image sets were used to map the tip vortices using epipolar analysis, a technique developed by Meyn and Bennett [143] and further used in conjunction with stereo BOS by Raffel et al. [144]. Though not a traditional BOS technique, a digital variation of Weinstein's streak camera method had been developed called LimbBOS. Here, the plane's passage across is time-resolved recording such that the shock waves that optically distort the Sun's edge (or *limb*) are revealed. By extracting the distorted outer perimeter of the sun from each frame in the sequence then aligning and spacing the

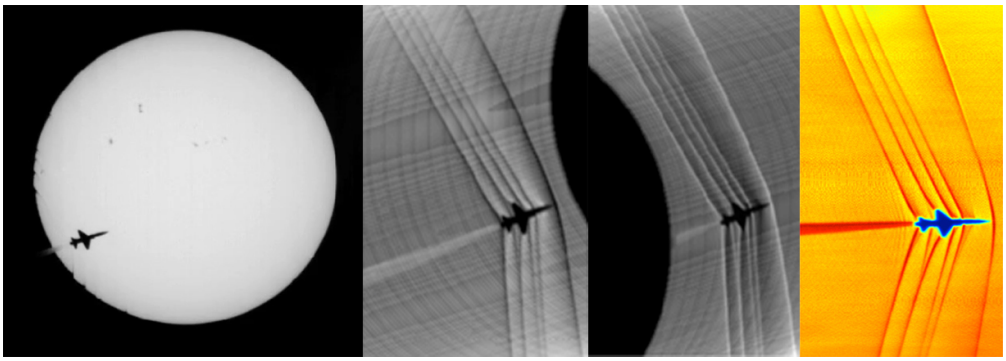

Fig. 17 Schlieren image construction method LimbBOS from the distorted perimeter of the sun caused by shockwaves of a T-38 at Mach 1.1.

sequence of solar "limb" rings into a composite, a schlieren image is constructed [141]. This technique is currently planned to capture the shock structure of the QueSST X-59 aircraft.

The airborne background oriented schlieren method (AirBOS) evolved from work done in wind tunnels and cooperative research with DLR Goettingen under the US Army-DLR Memorandum of Understanding from 2000 to 2012. Conceptually simple: a slow-flying observer aircraft at high altitude records the passage of a supersonic aircraft over the natural flora of the Mojave Desert, where frames from the sequence before the aircraft enters the field of view are used as references for the frames with the aircraft present. The first campaign took place in 2012 using a low-resolution Visible/SWIR camera - this was the only camera cleared for flight at the time. The pixel size pitch was 25 microns and the frame rate was 130 fps. The field of view was not optimized. All of these factors worked against the success of obtaining a quality schlieren image, however the proof of the AirBOS concept was achieved. The very first pass yielded a result. Out of this data, a smart averaging method was developed, where the BOS images were aligned to the aircraft in each image, and simply averaged. Additionally, reference alignment using projective transform "dewarping" was applied to each image to compensate for pitch, yaw, and roll variances of the observer aircraft. This became the default alignment method for all subsequent AirBOS work. Unfortunately this data was classified and never published.

The next AirBOS campaign occurred in 2014, where two 4 megapixel high speed cameras were deployed. The area in the Black Mountain Supersonic Corridor, the flight test range operated by Edwards Air Force Base, was systematically searched using Google Earth and subsequent flights where the "sweet spot" was imaged and evaluated using the flight cameras prior to a test flight. The altitude for the observer was set at the highest practical for the KingAir, 30,000 feet. The magnification of the flora was based on averaged measurements of bushes, where the lens selection rendered the bushes over 3-5 pixels. The frame rate of the camera permitted a large number of image samples to apply the cross-correlation BOS processing method. This large image sequence - no less than 200 images - allowed smart averaging of the BOS image sequence. The noise reduction from averaging was sufficient to reveal the most detailed in-flight schlieren images to date. This success inspired the development of methods allowing for similar image sequences to be obtained in wind tunnel settings by projected and moving background patterns [145, 146].

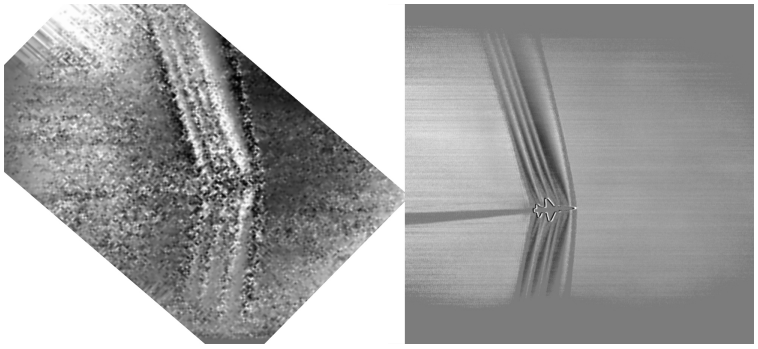

Fig. 18 Cross-correlation processed image (left) and optical-flow processed schlieren results (right) of a BOSCO image sequence.

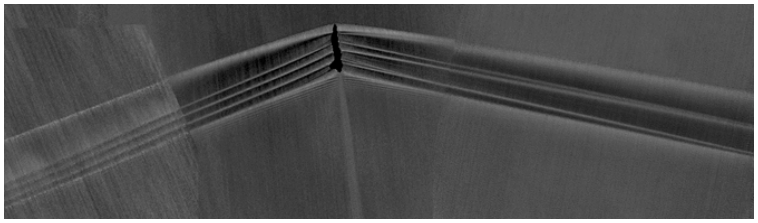

Fig. 19 Three BOSCO images aligned to capture an extended view of the T-38 shock structure.

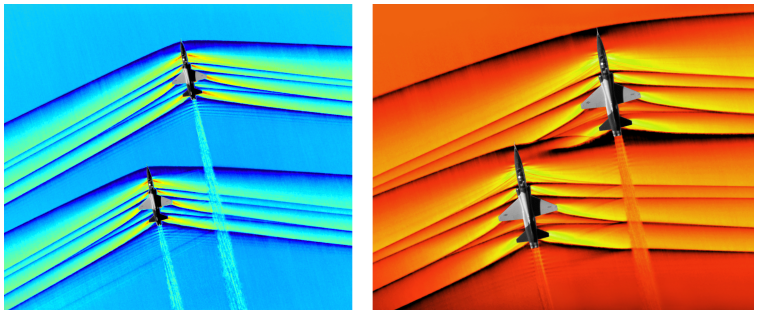

Fig. 20 AirBOS images of shock/jet exhaust and shock/shock interactions.

Concurrent with the aforementioned AirBOS campaign, Hill and Haering devised the BOSCO method [141]. Flight planning was challenging, as the pilot had to fly at supersonic speeds though a 50-meter window to eclipse the sun for the telescope view from the ground. The air-gapped etalon in their telescope provided sufficient visual texture, but the area and number of usable frames was quite small for the cross-correlation method to produce a schlieren image of value, so a Lucas-Kanade optical flow algorithm was applied and produced a clear schlieren image (Fig. 18). The BOSCO team then used three telescopes placed at 30-meter intervals on the ground to capture a larger area of the shock structure (Fig. 19).

After the clear advantage of using optical flow algorithms was demonstrated on the BOSCO data, Smith et al. [147] worked to optimize AirBOS data processing. One key innovation was averaging of multiple reference images to reduce noise generated in a single reference image, because the noise averages to zero. Improvements in a single image data solution was demonstrated when very weak Mach wave radiation was rendered. In 2018 the last AirBOS campaign sought to capture two supersonic aircraft flying in close formations to investigate shock-shock and shock-jet exhaust interactions. This work supported risk reduction of a potential amplification caused by a shock-jet exhaust interaction in the X-59 sonic signature. Using the same set of cameras as previous campaign, AirBOS images of the passage of two T-38s at varying distances were captured. In the images of Fig. 20, note the reflection of the tail shock off the exhaust plume of the lead aircraft. This reflection counters the results from cold-flow jet simulation performed in a supersonic wind tunnel, and its accompanying CFD analysis of that experiment [148].

VII. Conclusions and Future Outlook

Since its invention in the year 2000 and the review article that followed fifteen years later, BOS has continued to grow both in terms of its user base and its applications and extensions. Its ease of use and lack of need for specialized equipment and training have encouraged its adoption across multiple disciplines, and its flexibility and ruggedness have permitted flow visualizations and measurements that would have been impractical or impossible with conventional schlieren imaging. While guidance regarding the experimental setup and processing algorithm has been published for some time, advice is provided in condensed form in this review, supported by optical theory. Recent extensions such as tomography, data assimilation, and event-based imaging are discussed in detail, which may lead to exciting applications and scientific advancements in the near future. Implementations of BOS in challenging environments such as large-scale ground test facilities, ballistics and explosives testing, and *in situ* imaging of aircraft in flight are presented as well.

Based on the progress of the past decade in terms of extending the capabilities for BOS and discovering new application modalities, it is very difficult to predict the trajectory of the technique, even in the near future. It is very

likely that as progress is made in the active field of data assimilation, BOS measurements will prove a logical partner. This could have tremendous impacts, as BOS imaging from multiple cameras would potentially produce not just a three-dimensional refractive index field for visualization purposes, but also the pressure, temperature, and/or velocity field for the entire flow. Because of the simplicity of the BOS technique which requires only optical access and sufficient illumination, such an innovation would almost assuredly enable a step change in aerodynamic science. The adaptation of event-based imaging to BOS could likewise produce rapid advancements in the field by significantly reducing the difficulties associated with high-speed imaging, including camera memory limitations and the need for sufficient illumination.

The technique's portability, affordability, and simplicity will continue to drive new applications in challenging environments. This likely includes further innovation in ballistics and explosives research, but also applications in fields such as environmental science, infectious disease, and industrial HVAC where flow visualization is paramount but very difficult with other traditional methods. BOS could also prove useful in underwater environments where refractive index changes can be very strong by employing deflection-sensing algorithms such as cross-correlation that can resolve displacements of several pixels. It is clear that BOS will remain a mainstay experimental technique for fluid dynamics and continue to grow in its usefulness in the years to come.

Appendix A. Electromagnetic Foundations of Schlieren

Section II.A provides a framework for the quantitative interpretation of schlieren data. However, it is also instructive to explore the foundations of schlieren imaging through Maxwell's equations. Gradients in the speed of light within a variable-index gas arise from interactions between electromagnetic waves and the gas molecules. When a light wave passes through the medium, molecular dipoles oscillate in response to the imposed electromagnetic field, re-radiating electromagnetic energy in turn. In the absence of free charges or currents, the resultant light wave maintains the same frequency as the incident wave but undergoes a phase shift. This shift reduces the wave's *group velocity* compared to its velocity in a vacuum, effectively "slowing" the wave. This phenomenon underpins the Lorentz–Lorenz and Gladstone–Dale equations discussed in Sec. II.A.

The speed of light in a medium is described by its refractive index, which, as we shall see, is proportional to the mean molecular polarizability, α, and mass density, ρ, of the medium. In gas-phase schlieren imaging, this relationship is typically expressed by Eq. (3) (the Gladstone–Dale relation), linking the refractive index to the local fluid density and composition. For a medium with a non-uniform distribution of n, geometric optics describes light propagation within the medium using rays. Starting from Maxwell's equations, this section outlines the derivation of the Gladstone–Dale equation as well as the ray equation of geometric optics, which leads to the deflection model in Eq. (9). While a full derivation is beyond the scope of this review, additional details can be found in the classical text of Born and Wolf, *Principles of Optics* [149].

A. Maxwell's Equations

Both derivations begin with Maxwell's equations, simplified for a non-conducting medium that is void of current and charge,

$$\nabla \cdot \underline{D} = 0 \tag{A1a}$$

$$\nabla \cdot \underline{B} = 0 \tag{A1b}$$

$$\nabla \times \underline{E} = -\frac{\partial \underline{B}}{\partial t} \tag{A1c}$$

$$\nabla \times \underline{H} = \frac{\partial \underline{D}}{\partial t}. \tag{A1d}$$

In this expression, $\underline{E}$ is the electric field, $\underline{D}$ is the electric displacement, $\underline{B}$ is the magnetic flux density, and $\underline{H}$ is the magnetic field intensity. The material properties of the medium are described by its permittivity, $\tilde{\varepsilon}$, and permeability, $\tilde{\mu}$, which which couple the electromagnetic fields to the material via the constitutive relationships

$$\underline{D} = \tilde{\varepsilon}\underline{E} \quad \text{and} \quad \underline{B} = \tilde{\mu}\underline{H}. \tag{A2}$$

Taking the curl of Eq. (A1c), applying the vector identity

$$\nabla \times \nabla \times \underline{A} = \nabla\left(\nabla \cdot \underline{A}\right) - \nabla^2 \underline{A}, \tag{A3}$$

where $\nabla^2 \equiv \nabla \cdot \nabla$ is the Laplacian, and substituting Eqs. (A1d) and (A2) we obtain

$$\nabla \times \nabla \times \underline{E} = -\frac{\partial(\nabla \times \underline{B})}{\partial t} \tag{A4}$$

$$\nabla \underbrace{(\nabla \cdot \underline{E})}_{=0} - \nabla^2 \underline{E} = -\frac{\partial}{\partial t}\left(\tilde{\mu}\tilde{\varepsilon}\frac{\partial \underline{E}}{\partial t}\right). \tag{A5}$$

This reduces to a wave equation,

$$\nabla^2 \underline{E} - \tilde{\mu}\tilde{\varepsilon}\frac{\partial^2 \underline{E}}{\partial t^2} = 0, \tag{A6}$$

with a wave speed of

$$c = \frac{1}{\sqrt{\tilde{\mu}\tilde{\varepsilon}}}. \tag{A7}$$

For electromagnetic waves in a vacuum, the speed of light c_0 is determined by the vacuum permeability $\tilde{\mu}_0$ and permittivity $\tilde{\varepsilon}_0$,

$$c_0 = \frac{1}{\sqrt{\tilde{\mu}_0\tilde{\varepsilon}_0}}. \tag{A8}$$

The wave speed in Eq. (A6) can be expressed in terms of the refractive index $n = c_0/c$. Additionally, the permeability and permittivity of a medium are related to their relative values and vacuum quantities,

$$\tilde{\varepsilon} = \tilde{\varepsilon}_\mathrm{r}\tilde{\varepsilon}_0 \quad \text{and} \quad \tilde{\mu} = \tilde{\mu}_\mathrm{r}\tilde{\mu}_0, \tag{A9}$$

where $\tilde{\varepsilon}_\mathrm{r}$ and $\tilde{\mu}_\mathrm{r}$ are the relative permittivity and permeability, respectively. For non-magnetic materials, $\tilde{\mu}_\mathrm{r} \approx 1$, so $\tilde{\mu} = \tilde{\mu}_0$. Substituting these relations yields

$$n = \left(\frac{\tilde{\mu}\tilde{\varepsilon}}{\tilde{\mu}_0\tilde{\varepsilon}_0}\right)^{1/2} \Rightarrow n^2 = \tilde{\varepsilon}_\mathrm{r}. \tag{A10}$$

This equality, known as the refractive index–permittivity relation, connects the macroscopic refractive index, n, to the relative permittivity of the medium, $\tilde{\varepsilon}_\mathrm{r}$.

B. Lorentz–Lorenz and Gladstone–Dale Equations

The speed of light in a medium depends on the interaction between the material and the incident electromagnetic wave, which can be described in terms of the medium's polarizability. Most gases encountered in schlieren imaging are dielectric materials, meaning they are electrical insulators whose molecules can be polarized by incident electromagnetic radiation. For a dielectric material, the displacement field is given by

$$\underline{D} = \tilde{\varepsilon}_0\underline{E} + \underline{P}, \tag{A11}$$

where $\underline{P}$ is the polarization density vector. In a linear dielectric medium, $\underline{P}$ is directly proportional to the electric field,

$$\underline{P} = \tilde{\varepsilon}_0\chi_\mathrm{e}\underline{E}, \tag{A12}$$

where χ_e is the electric susceptibility, which is a macroscopic quantity. The relative permittivity, introduced earlier, is related to the electric susceptibility as follows,

$$\tilde{\varepsilon}_\mathrm{r} = 1 + \chi_\mathrm{e}. \tag{A13}$$

This relationship is valid for most schlieren scenarios. For waves of greater intensity, however, higher-order terms in $\underline{E}$ become significant, which is the subject of non-linear optics.

The local field around a single molecule in a medium, $\underline{E}'$, differs from the macroscopic field, $\underline{E}$, due to contributions from induced fields within the medium. Assuming the medium is locally isotropic and homogeneous, and neglecting interactions between neighboring dipoles, the local field is given by

$$\underline{E}' = \underline{E} + \frac{1}{3\tilde{\varepsilon}_0}\underline{P} \tag{A14}$$

This relation accounts for the macroscopic field and the induced field within a spherical cavity centered on the molecule. The polarization density is proportional to the dipole moment density, $\underline{p}$, which in turn depends on the *local* field,

$$\underline{P} = N\underline{p} = N\alpha\underline{E}', \tag{A15}$$

where N is the number density of molecules and α is the mean molecular polarizability.

While the polarizability of a medium, represented by $\boldsymbol{\alpha}$, is generally a rank-2 tensor, for isotropic media with randomly-oriented molecules it reduces to an average scalar value, α, a microscopic property. In contrast, $\underline{P}$ is a macroscopic quantity that is dependent upon the applied field, $\underline{E}$, and number density, N. Note as well that α varies with the wavelength of light, changing significantly near wavelengths corresponding to electronic, vibrational, or rotational transitions of the molecule. Away from these transitions, the wavelength dependence of α is smooth, resulting in a moderate wavelength dependence of n that gives rise to chromatic dispersion.

Substituting Eq. (A15) into Eq. (A14) and solving for $\underline{P}$, we find that

$$\underline{P} = N\alpha\left(\underline{E} + \frac{1}{3\tilde{\varepsilon}_0}\underline{P}\right) = \frac{N\alpha\underline{E}}{1 - (N\alpha/3\tilde{\varepsilon}_0)}. \tag{A16}$$

Using Eq. (A12) for $\underline{P}$, the electric susceptibility χ_e is given by

$$\tilde{\varepsilon}_0\chi_\mathrm{e}\underline{E} = \frac{N\alpha\underline{E}}{1 - (N\alpha/3\tilde{\varepsilon}_0)} \iff \chi_\mathrm{e} = \frac{(N\alpha/\tilde{\varepsilon}_0)}{1 - (N\alpha/3\tilde{\varepsilon}_0)}. \tag{A17}$$

Relating this to the refractive index via Eqs. (A10) and (A13), i.e. $\chi_\mathrm{e} = n^2 - 1$, leads to

$$n^2 - 1 = \frac{(N\alpha/\tilde{\varepsilon}_0)}{1 - (N\alpha/3\tilde{\varepsilon}_0)}. \tag{A18}$$

Adding three to both sides gives

$$n^2 + 2 = \frac{3}{1 - (N\alpha/3\tilde{\varepsilon}_0)}, \tag{A19}$$

such that

$$\frac{n^2 - 1}{n^2 + 2} = \frac{N\alpha}{3\tilde{\varepsilon}_0}, \tag{A20}$$

which is the well-known Lorentz–Lorenz equation. When this equation is written in terms of $\tilde{\varepsilon}_r$ instead of n^2, it is called the Clausius–Mossotti relation. Using the Ideal Gas Law, the number density N is related to the mass density ρ as

$$N = \frac{\tilde{N}_\mathrm{A}}{W}\rho, \tag{A21}$$

where $\tilde{N}_\mathrm{A}$ is Avogadro's number and W is the molar mass of the mixture. Therefore, the Lorentz–Lorenz equation is

$$\frac{1}{\rho}\frac{n^2 - 1}{n^2 + 2} = \frac{\tilde{N}_\mathrm{A}\alpha}{3W\tilde{\varepsilon}_0} \iff \frac{1}{\rho}\frac{n^2 - 1}{n^2 + 2} = \frac{A}{W}, \tag{A22}$$

and the molar refractivity can be expressed in terms of microscopic quantities as

$$A = \frac{\tilde{N}_\mathrm{A}\alpha}{3\tilde{\varepsilon}_0}. \tag{A23}$$

It is important to note that this derivation uses SI units. However, Maxwell's equations are often expressed in Gaussian units (a subsystem of CGS units). In this case, the mean molecular polarizability, denoted as α' in Gaussian units for clarity, is related to the SI version by

$$\alpha' = \frac{\alpha}{4\pi\tilde{\varepsilon}_0}. \tag{A24}$$

Equation (A22) underscores the fundamental relationship between molecular polarizability and refractive index variations, linking them to gas properties such as ρ, N, p, and T, which are interconnected through an equation of state.

For gases, the refractive index is close to unity. Expanding $n^2 - 1$ about 1 using a first-order Taylor series yields $2(n-1)$, while $n^2 + 2 \approx 3$. Inserting these approximations into the Lorentz–Lorenz equation, we obtain

$$n = 1 + \frac{N\alpha}{2\tilde{\varepsilon}_0}. \tag{A25}$$

Using the Ideal Gas Law once again, we obtain the Gladstone–Dale relation,

$$n = 1 + \frac{\tilde{N}_\mathrm{A}\alpha}{2M\tilde{\varepsilon}_0}\rho \iff n = 1 + G\rho, \tag{A26}$$

where the fundamental definition of the Gladstone–Dale coefficient is

$$G = \frac{\tilde{N}_\mathrm{A}\alpha}{2W\tilde{\varepsilon}_0}. \tag{A27}$$

Finally, we emphasize once again that α, being a wavelength-dependent property, introduces a moderate wavelength dependence in n for most gases at visible wavelengths.

C. Ray Equation of Geometric Optics

Geometric optics describes the behavior of light in the limit where its wavelength is vanishingly small. This approximation is valid when the wavelength is negligible relative to both the length scale of refractive index gradients in the transmission medium and the physical dimensions of optical components. This condition is virtually always satisfied in schlieren imaging, where the refractive index field varies smoothly over distances much larger than the wavelength of visible light. In this regime, light propagation can be modeled using rays, and electromagnetic energy travels along paths perpendicular to the wavefronts of n. These paths are described by the ray equation of geometric optics. Importantly, this approximation assumes that phase coherence is maintained, while the wave nature of light, including diffraction and interference, is not considered. Geometric optics provides an effective framework for modeling schlieren phenomena, wherein wave effects are negligible.

Our derivation of the ray equation begins with a time-harmonic ansatz for the electric field,

$$\underline{E}(\underline{r}, t) = \underline{E}_0(\underline{r})\, e^{-\mathrm{i}\omega t}, \tag{A28}$$

where $\underline{r}$ is a position vector, i is the imaginary number, and $\omega = 2\pi c/\lambda$ is the angular frequency of a light wave with wavelength λ. Substituting this ansatz into the wave equation derived from Maxwell's equations, i.e. Eq. (A6),

$$\nabla^2 \underline{E}_0\, e^{-\mathrm{i}\omega t} + \tilde{\mu}\tilde{\varepsilon}\omega^2 \underline{E}_0\, e^{-\mathrm{i}\omega t} = 0, \tag{A29}$$

Factoring out the exponential term, we arrive at

$$\nabla^2 \underline{E}_0 + k^2 n^2 \underline{E}_0 = 0. \tag{A30}$$

where $k = \omega/c_0$ is the free-space wavenumber and $n^2 = \tilde{\mu}\tilde{\varepsilon}c_0^2$. This is called the Helmholtz equation.

Next, we decompose the electric field into a slowly varying amplitude, $\underline{A}$, and a rapidly oscillating phase, $\mathcal{S}$, the latter of which is known as the eikonal:

$$\underline{E}_0(\underline{r}) = \underline{A}(\underline{r})\, e^{\mathrm{i}k\mathcal{S}(\underline{r})}. \tag{A31}$$

Plugging this decomposition into the Helmholtz equation gives

$$\nabla^2\left(\underline{A}e^{\mathrm{i}k\mathcal{S}}\right) + k^2 n^2 \underline{A} e^{\mathrm{i}k\mathcal{S}} = 0. \tag{A32}$$

We use the Laplacian product rule,

$$\nabla^2(\varphi\underline{A}) = \left(\nabla^2\varphi\right)\underline{A} + 2\left(\nabla\varphi\cdot\nabla\right)\underline{A} + \varphi\nabla^2\underline{A}, \tag{A33}$$

substituting $\varphi = e^{\mathrm{i}k\mathcal{S}}$ and utilizing $\nabla e^{\mathrm{i}k\mathcal{S}} = \mathrm{i}k\left(\nabla\mathcal{S}\right)e^{\mathrm{i}k\mathcal{S}}$ and $\nabla^2 e^{\mathrm{i}k\mathcal{S}} = \left(\mathrm{i}k\left(\nabla\mathcal{S}\right) - k^2\left(\nabla\mathcal{S}\right)^2\right)e^{\mathrm{i}k\mathcal{S}}$. Expanding the Helmholtz equation via Eq. (A33) and including these terms, we have

$$\left(\mathrm{i}k\left(\nabla^2\mathcal{S}\right)\underline{A} - k^2\left(\nabla\mathcal{S}\right)^2\underline{A} + 2\mathrm{i}k\left(\nabla\mathcal{S}\cdot\nabla\underline{A}\right) + \nabla^2\underline{A}\right)e^{\mathrm{i}k\mathcal{S}} + k^2 n^2 \underline{A} e^{\mathrm{i}k\mathcal{S}} = 0. \tag{A34}$$

We can factor out the exponential quantities. Moreover, for large k (i.e. small λ), the expression is dominated by k^2-order terms,

$$-k^2 \left(\nabla \mathcal{S}\right)^2 \underline{A} e^{\mathrm{i}k\mathcal{S}} + k^2 n^2 \underline{A} e^{\mathrm{i}k\mathcal{S}} \approx 0, \tag{A35}$$

which simplifies to the eikonal equation,

$$\nabla \mathcal{S} \cdot \nabla \mathcal{S} = n^2. \tag{A36}$$

This equation describes the relationship between the refractive index, n, and the eikonal, $\mathcal{S}$, where isosurfaces of $\mathcal{S}$ are wavefronts of the refractive index field.

To describe the trajectory of light rays, we introduce the wavevector $\underline{k}$, which is perpendicular to the wavefronts,

$$\underline{k} = \nabla \mathcal{S}. \tag{A37}$$

From the eikonal equation, we see that the magnitude of the wavevector is $|\underline{k}| = n$. Since light rays propagate in the direction of the wavevector, we can write

$$\underline{k} = n \frac{\partial \underline{r}}{\partial s}, \tag{A38}$$

where $\partial \underline{r}/\partial s$ is a unit vector tangent to the ray and s is the arc length along the ray. Based on the definition in Eq. (A38) and $|\underline{k}| = n$, the derivative along the ray path must be

$$\frac{\underline{k} \cdot \nabla}{n} = \frac{\partial}{\partial s}. \tag{A39}$$

Using these elements, we derive the ray equation by taking the gradient of the eikonal equation,

$$\nabla \left(\nabla \mathcal{S} \cdot \nabla \mathcal{S}\right) = \nabla n^2 \tag{A40}$$

$$2 \left(\underline{k} \cdot \nabla\right) \underline{k} = 2n \nabla n. \tag{A41}$$

Substituting our wavevector relations from Eqs. (A38) and (A39) and simplifying, we find

$$\frac{\partial}{\partial s}\left(n \frac{\partial \underline{r}}{\partial s}\right) = \nabla n, \tag{A42}$$

which is the ray equation of geometric optics. Invoking the small angle approximation and $n \approx n_0$ from Sec. II.A, we can integrate the ray equation to determine the net change in the ray's direction,

$$\underline{\varepsilon} \approx \left(\frac{\partial \underline{r}}{\partial s}\right)_{\text{out}} - \left(\frac{\partial \underline{r}}{\partial s}\right)_{\text{in}} = \frac{1}{n_0} \int \nabla n \, \mathrm{d}s. \tag{A43}$$

Here, the subscripts "in" and "out" denote the ray direction as it enters and exits the phase object, respectively.

Appendix B. Mixture-Averaged Coefficients

While most BOS experiments involve gases with a uniform composition, such as homogeneous air flows, the technique is increasingly applied to flows with variable mixtures, like flames. In these scenarios, the relationship between the refractive index, n, and the mass density, ρ, or between n and the molar concentration, C, can vary significantly with the composition of the gas. This appendix provides an overview of these relationships, emphasizing their dependence on the gas composition. Additionally, it includes tabulated data to calculate G and A for various species.

A. Mass- and Mole-Fraction-Weighted Coefficients

To begin, it is helpful to recall the mass and molar forms of the Gladstone–Dale relation,

$$n = 1 + G\rho \tag{B1a}$$

$$n = 1 + \frac{3A}{2} C, \tag{B1b}$$

where the molar concentration is $C = \rho/W$. Similarly, the Lorentz–Lorenz equation can be written in mass and molar forms,

$$\frac{1}{\rho}\frac{n^2-1}{n^2+2} = \frac{2G}{3} \tag{B2a}$$

$$\frac{1}{C}\frac{n^2-1}{n^2+2} = A. \tag{B2b}$$

Species-specific Gladstone–Dale coefficients, G_i, and molar refractivities, A_i, for the i^{th} species are used to calculate the corresponding mixture properties as follows,

$$G = \sum_i Y_i G_i \tag{B3a}$$

$$A = \sum_i X_i A_i, \tag{B3b}$$

where Y_i and X_i denote the mass and mole fractions of the i^{th} species, respectively. The equivalence of these mixture expressions can be understood using the following relationships,

$$\rho = WC = \frac{WN}{\tilde{N}_{\text{A}}} \tag{B4a}$$

$$G \approx \frac{3A}{2W} \iff A \approx \frac{2}{3}WG \tag{B4b}$$

$$W = \sum_i X_i W_i, \tag{B4c}$$

where W_i is the molecular weight of the i^{th} species. Using these relations, the Gladstone–Dale coefficient of a mixture can be expressed as

$$G = \frac{3}{2W}\underbrace{\sum_i X_i A_i}_{A} = \sum_i \frac{X_i W_i G_i}{W} = \sum_i \underbrace{\frac{X_i W_i}{W}}_{Y_i} G_i. \tag{B5}$$

Thus, the mass-fraction-weighted Gladstone–Dale coefficient is consistent with the mole-fraction-weighted molar refractivity.

B. Some Refractive Index Data

If the composition of a gas is known, its effective Gladstone–Dale coefficient and molar refractivity can be calculated using a weighted sum of species-specific values, as shown in Eq.(B3). These coefficients can then be used to determine the refractive index via Eq. (B1) or (B2). We note that the Gladstone–Dale equation is an approximation of the Lorentz–Lorenz equation, which can be solved analytically,

$$n = \sqrt{\frac{1+2CA}{1-CA}}, \tag{B6}$$

but this expression is rarely used in quantitative schlieren work due to the complexity introduced when differentiating it with respect to C (or ρ). However, while the Gladstone–Dale approximation is generally sufficient in BOS, it becomes invalid in cases where n is large. For this reason, we provides data for both A and G in this section, as well as some guidance on their computation.

The most commonly used gas in BOS experiments is air, and one of the most accurate refractive index formulas for dry air is Ciddor's formula [150]. This formula applies to air at $T_0 = 288.15$ K, $p_0 = 1$ atm, and 450 ppm of CO_2, and it is expressed as

$$n = 1 + \frac{\beta_1}{\beta_2 - \lambda^2} + \frac{\beta_3}{\beta_4 - \lambda^2}, \tag{B7}$$

where the coefficients are

$$\beta_1 = 5.792105 \times 10^{-8} \tag{B8a}$$

$$\beta_2 = 2.38019 \times 10^{-4} \tag{B8b}$$

$$\beta_3 = 1.67917 \times 10^{-9} \tag{B8c}$$

$$\beta_4 = 5.7362 \times 10^{-5}, \tag{B8d}$$

with all units in nm^{-2}, and λ is in nm. This expression is valid from 230–1690 nm. The implied Gladstone–Dale coefficient is

$$G = \left(\frac{\beta_1}{\beta_2 - \lambda^2} + \frac{\beta_3}{\beta_4 - \lambda^2} \right) \rho_{\mathrm{air},0}^{-1}, \tag{B9}$$

where $\rho_{\mathrm{air},0} \approx 1.2248\ \mathrm{kg/m^3}$. Similarly, the molar refractivity can be calculated by substituting Eq. (B7) into Eq. (B2b), with $C_{\mathrm{air},0} \approx 4.2292 \times 10^{-5}\ \mathrm{cm^3/mol}$.

Mixture effects on G and A are particularly significant in many combustion processes. A classical reference for refractive index data for combustion-relevant species is that of Gardiner et al. [151], which is summarized in Table 1. The authors provided two sets of data: one based on experimental measurements and another derived from theoretical calculations. For species appearing in both tables, the experimental data are included in Table 1. Gardiner et al. determined Cauchy dispersion coefficients for each species, allowing n_0 to be calculated as a function of wavelength via the following equation:

$$n^\circ = 1 + \frac{\beta_1}{\beta_2 - \lambda^2}. \tag{B10}$$

Once again, λ is in nm and β_1 and β_2 are in nm^{-2}. The reference conditions for n_0 is $T_0 = 273.15$ K and $p = 1$ atm. Values of these parameters for selected species are presented in Table 1. The Table also reports values of G and A at three wavelengths, corresponding to the output of an N_2 laser (337.1 nm), a doubled Nd:YAG (532.0 nm), and a HeNe laser (632.8 nm). The fitted dispersion formulas are valid over the range 337.1–694.3 nm. While Gardiner's data remain a valuable resource, it is important to note that many of the results are derived from theoretical calculations that rely on

Table 1 Selected Gladstone–Dale Coefficients, and Molar Refractivities of Combustion-Relevant Gases

Species	W g/mol	$\beta_1 \times 10^{10}$ nm^{-2}	$\beta_2 \times 10^4$ nm^{-2}	$G \times 10^4$, $\mathrm{m^3/kg}$			A, $\mathrm{cm^3/mol}$		
				337 nm	*532 nm*	*632 nm*	*337 nm*	*532 nm*	*632 nm*
C_2H	25.03	457.31	0.8638	5.28	4.94	4.88	8.81	8.25	8.15
C_2H_2	26.04	425.54	0.7504	5.53	5.12	5.05	9.6	8.89	8.76
C_2H_4	28.05	603.59	0.8721	6.15	5.76	5.69	11.5	10.78	10.65
C_2H_6	30.07	1020.87	1.3771	5.9	5.67	5.63	11.83	11.37	11.28
C_3H_6	42.08	967.01	0.9478	5.99	5.64	5.58	16.8	15.83	15.66
C_3H_8	44.09	1406.25	1.3345	5.73	5.5	5.46	16.85	16.17	16.04
CH	13.02	291.26	1.2329	4.38	4.19	4.15	3.8	3.63	3.6
CH_3	15.04	525.39	1.4124	5.91	5.69	5.64	5.93	5.7	5.66
CH_4	16.04	559.53	1.2964	6.47	6.2	6.15	6.92	6.63	6.58
CO	28.01	404.39	1.2356	2.82	2.7	2.67	5.27	5.03	4.99
CO_2	44.01	681.39	1.5571	2.36	2.28	2.26	6.93	6.69	6.65
H	1.01	87.47	0.7839	27.95	25.99	25.63	1.88	1.75	1.72
H_2	2.02	187.53	1.3783	16.16	15.52	15.41	2.17	2.09	2.07
H_2O	18.02	291.48	1.1869	3.3	3.15	3.12	3.96	3.78	3.75
HO	17.01	105.76	0.3209	5.98	4.88	4.71	6.78	5.53	5.34
N_2	28.01	562.45	1.9097	2.47	2.4	2.39	4.61	4.48	4.46
NO	30.01	393.4	1.3648	2.3	2.21	2.19	4.6	4.42	4.39
O	16	71.63	0.6049	1.94	1.76	1.73	2.07	1.88	1.85
O_2	32	380.37	1.4334	1.98	1.91	1.89	4.22	4.07	4.04

significant assumptions. For applications demanding high precision, it is advisable to consult more recent studies or experimentally verified data.

Acknowledgments

B.E.S. acknowledges support from the National Institute of Biomedical Imaging and Bioengineering (NIBIB) grant no. 1-R21-EB032644-01 and the National Science Foundation (NSF) under grant no. CBET-2227764. S.J.G. also acknowledges support from NSF under the same grant, and he acknolwedges helpful feedback from Mr. Joseph Molnar and Mr. Reese Peck Cowles. B.F.B. acknowledges the support of NASA's Transformational Tools & Technologies (T^3) and Aerosciences Evaluation & Test Capabilities Projects as well as the assistance of Mr. Wayne Page, Mr. Stephen Jones, and Dr. Joshua Weisberger. The use of trademarks or names of manufacturers in this report is for accurate reporting and does not constitute an official endorsement, either expressed or implied, of such products or manufacturers by the National Aeronautics and Space Administration.

References

[1] Settles, G. S., *Schlieren and Shadowgraph Techniques*, 1st ed., Springer Berlin Heidelberg, 2001.

[2] Foucault, L., "Memoire sur la construction des telescopes en verre argente," *Annales de l'Observatoire de Paris*, Vol. 5, 1859, pp. 197–237.

[3] Toepler, A. J. I., *Beobachtungen nach einer neuen optischen methode: Ein beitrag experimentalphysik*, 157, W. Engelmann, 1906.

[4] Schardin, H., "Schlieren methods and their application," *Ergbnisse der Exakten Naturwissenschaften*, Vol. 20, 1942, pp. 303–439.

[5] Dalziel, S. B., Hughes, G. O., and Sutherland, B. R., "Whole-field density measurements by 'synthetic schlieren'," *Experiments in Fluids*, Vol. 28, No. 4, 2000, pp. 322–335. https://doi.org/10.1007/s003480050391.

[6] Raffel, M., Richard, H., and Meier, G. E. A., "On the applicability of background oriented optical tomography for large scale aerodynamic investigations," *Experiments in Fluids*, Vol. 28, No. 5, 2000, pp. 477–481. https://doi.org/10.1007/s003480050408.

[7] Meier, G. E. A., "Computerized background-oriented schlieren," *Experiments in Fluids*, Vol. 33, No. 1, 2002, pp. 181–187. https://doi.org/10.1007/s00348-002-0450-7.

[8] Richard, H., Raffel, M., Rein, M., Kompenhans, J., and Meier, G. E. A., "Demonstration of the applicability of a Background Oriented Schlieren (BOS) method," *Laser Techniques for Fluid Mechanics*, 2002, pp. 145–156. https://doi.org/10.1007/978-3-662-08263-8_9.

[9] Raffel, M., Tung, C., Richard, H., Yu, Y., and Meier, G. E. A., "Background oriented stereoscopic schlieren (BOSS) for full-scale helicopter vortex characterization," *The Millennium 9th International Symposium on Flow Visualization*, University Edinburgh, 2000, pp. 450.1–450.11.

[10] Raffel, M., "Background-oriented schlieren (BOS) techniques," *Experiments in Fluids*, Vol. 56, No. 3, 2015. https://doi.org/10.1007/s00348-015-1927-5.

[11] Gladstone, J. H., and Dale, T. P., "Researches on the refraction, dispersion, and sensitiveness of liquids," *Phil. Trans. R. Soc.*, Vol. 153, 1863, pp. 317–343. https://doi.org/10.1098/rstl.1863.0014.

[12] Richard, H., and Raffel, M., "Principle and Applications of the Background Oriented Schlieren (BOS) Method," *Measurement Science and Technology*, Vol. 12, 2001, pp. 1576–1585. https://doi.org/10.1088/0957-0233/12/9/325.

[13] Debrus, S., Francon, M., Grover, C., May, M., and Robin, M., "Ground glass differential interferometer," *Applied Optics*, Vol. 11, 1972, pp. 853–858.

[14] Köpf, U., "Application of speckling for measuring the deflection of laser light by phase objects," *Optics Communications*, Vol. 5, No. 5, 1972, pp. 347–350. https://doi.org/10.1016/0030-4018(72)90030-2.

[15] Wernekinck, U., and Merzkirch, W., "Speckle photography of spatially extended refractive-index fields," *Applied Optics*, Vol. 26, No. 1, 1987, p. 31. https://doi.org/10.1364/ao.26.000031.

[16] Rajendran, L., Zhang, J., Bane, S., and Vlachos, P., "Uncertainty-based weighted least squares density integration for background-oriented schlieren," *Experiments in Fluids*, Vol. 61, No. 11, 2020. https://doi.org/10.1007/s00348-020-03071-w.

[17] Settles, G. S., and Hargather, M. J., "A review of recent developments in schlieren and shadowgraph techniques," *Measurement Science and Technology*, Vol. 28, No. 4, 2017. https://doi.org/10.1088/1361-6501/aa5748.

[18] Torres, S. M., Kimberley, J., and Hargather, M. J., "Stress field measurements using quantitative schlieren," *Journal of Applied Physics*, Vol. 136, No. 9, 2024. https://doi.org/10.1063/5.0223560.

[19] Agrawal, A. K., Butuk, N. K., Gollahalli, S. R., and Griffin, D., "Three-dimensional rainbow schlieren tomography of a temperature field in gas flows," *Applied Optics*, Vol. 37, No. 3, 1998, pp. 479–485.

[20] Settles, G. S., "Full-Scale Schlieren Flow Visualization," *The 7th International Symposium on Flow Visualization*, 1995.

[21] Weinstein, L. M., "An Optical Technique for Examining Aircraft Shock Wave Structures in Flight," *High-Speed Research: 1994 Sonic Boom Workshop*, 1994.

[22] Weinstein, L. M., "Review and update of lens and grid schlieren and motion camera schlieren," *The European Physical Journal Special Topics*, Vol. 182, No. 1, 2010, pp. 65–95.

[23] Heineck, J. T., Banks, D. W., Smith, N. T., Schairer, E. T., Bean, P. S., and Robillos, T., "Background-Oriented Schlieren Imaging of Supersonic Aircraft in Flight," *AIAA Journal*, Vol. 59, No. 1, 2021. https://doi.org/10.2514/1.j059495.

[24] Zitová, B., and Flusser, J., "Image registration methods: a survey," *Image and Vision Computing*, Vol. 21, No. 11, 2003, pp. 977–1000. https://doi.org/10.1016/s0262-8856(03)00137-9.

[25] Horn, B. K. P., and Schunck, B. G., "Determining Optical Flow," *Artificial Intelligence*, Vol. 17, 1981, pp. 185–203. https://doi.org/10.1016/0004-3702(81)90024-2.

[26] Atcheson, B., Heidrich, W., and Ihrke, I., "An evaluation of optical flow algorithms for background oriented schlieren imaging," *Experiments in Fluids*, Vol. 46, No. 3, 2009, pp. 467–476.

[27] Schmidt, B. E., and Woike, M. R., "Wavelet-based optical flow analysis (wOFA) for background oriented schlieren (BOS) image processing," *AIAA Journal*, Vol. 59, No. 8, 2021. https://doi.org/10.2514/1.J060218.

[28] Rajendran, L. K., Bane, S. P. M., and Vlachos, P. P., "Dot tracking methodology for background-oriented schlieren (BOS)," *Experiments in Fluids*, Vol. 60, No. 11, 2019. https://doi.org/10.1007/s00348-019-2793-3.

[29] Wernet, M. P., "Real-time background oriented schlieren with self-illuminated speckle background," *Measurement Science and Technology*, Vol. 31, No. 1, 2019. https://doi.org/10.1088/1361-6501/ab4211.

[30] Meinhart, C. D., Wereley, S. T., and Santiago, J. G., "A PIV Algorithm for Estimating Time-Averaged Velocity Fields," *Journal of Fluids Engineering*, Vol. 122, No. 2, 2000, pp. 285–289. https://doi.org/10.1115/1.483256.

[31] Raffel, M., Smith, N. T., Wolf, C. C., Heineck, J. T., and Gardner, A. D., "Projected moving patterns for reference-free background-oriented schlieren technique (BOS)," *Measurement Science and Technology*, Vol. 35, No. 11, 2024. https://doi.org/10.1088/1361-6501/ad7165.

[32] Pan, B., Asundi, A., Xie, H., and Gao, J., "Digital image correlation using iterative least squares and pointwise least squares for displacement field and strain field measurements," *Optics and Lasers in Engineering*, Vol. 47, No. 7–8, 2009, pp. 865–874. https://doi.org/10.1016/j.optlaseng.2008.10.014.

[33] Lucas, B., and Kanade, T., "An iterative image registration technique with an application to stereo vision," *Proceedings of the 7th international joint conference on artificial intelligence*, 1981, pp. 674–679. https://doi.org/10.5555/1623264.1623280.

[34] Mercier, B., and Lacassagne, T., "Design rules for Background Oriented Schlieren experiments with least-squares based displacement calculation," *Flow Measurement and Instrumentation*, Vol. 92, 2023. https://doi.org/10.1016/j.flowmeasinst.2023.102395.

[35] Grauer, S. J., and Steinberg, A. M., "Fast and robust volumetric refractive index measurement by unified background-oriented schlieren tomography," *Experiments in Fluids*, Vol. 61, No. 3, 2020. https://doi.org/10.1007/s00348-020-2912-1.

[36] Wildeman, S., "Real-time quantitative schlieren imaging by fast Fourier demodulation of a checkered backdrop," *Experiments in Fluids*, Vol. 59, No. 6, 2018. https://doi.org/10.1007/s00348-018-2553-9.

[37] Shimazaki, T., Ichihara, S., and Tagawa, Y., "Background oriented schlieren technique with fast Fourier demodulation for measuring large density-gradient fields of fluids," *Experimental Thermal and Fluid Science*, Vol. 134, 2022. https://doi.org/10.1016/j.expthermflusci.2022.110598.

[38] Vinnichenko, N. A., Pushtaev, A. V., Plaksina, Y. Y., and Uvarov, A. V., "Performance of Background Oriented Schlieren with different background patterns and image processing techniques," *Experimental Thermal and Fluid Science*, Vol. 147, 2023. https://doi.org/10.1016/j.expthermflusci.2023.110934.

[39] Perlman, E., Burns, R., Li, Y., and Meneveau, C., "Data exploration of turbulence simulations using a database cluster," *Proceedings of the 2007 ACM/IEEE conference on Supercomputing - SC '07*, 2007. https://doi.org/10.1145/1362622.1362654.

[40] Li, Y., Perlman, E., Wan, M., Yang, Y., Meneveau, C., Burns, R., Chen, S., Szalay, A., and Eyink, G., "A public turbulence database cluster and applications to study Lagrangian evolution of velocity increments in turbulence," *Journal of Turbulence*, Vol. 9, 2008, p. N31. https://doi.org/10.1080/14685240802376389.

[41] Thielicke, W., and Stamhuis, E. J., "PIVlab - Towards User-friendly, Affordable and Accurate Digital Particle Image Velocimetry in MATLAB," *Journal of Open Research Software*, Vol. 2, 2014. https://doi.org/10.5334/jors.bl.

[42] Schwarz, C., and Braukmann, J. N., "Practical aspects of designing background-oriented schlieren (BOS) experiments for vortex measurements," *Experiments in Fluids*, Vol. 64, No. 4, 2023. https://doi.org/10.1007/s00348-023-03602-1.

[43] Goldhahn, E., and Seume, J., "The background oriented schlieren technique: sensitivity, accuracy, resolution and application to a three-dimensional density field," *Experiments in Fluids*, Vol. 43, No. 2–3, 2007, pp. 241–249. https://doi.org/10.1007/s00348-007-0331-1.

[44] Gojani, A. B., and Obayashi, S., "Assessment of some experimental and image analysis factors for background-oriented schlieren measurements," *Applied Optics*, Vol. 51, No. 31, 2012. https://doi.org/10.1364/ao.51.007554.

[45] Hargather, M. J., and Settles, G. S., "A comparison of three quantitative schlieren techniques," *Optics and Lasers in Engineering*, Vol. 50, No. 1, 2012. https://doi.org/10.1016/j.optlaseng.2011.05.012.

[46] Greenleaf, A. R., *Photographic Optics*, MacMillan, 1950.

[47] Schwarz, C., Bauknecht, A., Wolf, C. C., Coyle, A., and Raffel, M., "A Full-Scale Rotor-Wake Investigation of a Free-Flying Helicopter in Ground Effect Using BOS and PIV," *Journal of the American Helicopter Society*, Vol. 65, No. 3, 2020, pp. 1–20. https://doi.org/10.4050/jahs.65.032007.

[48] Venkatakrishnan, L., and Meier, G. E. A., "Density measurements using the background oriented schlieren technique," *Experiments in Fluids*, Vol. 37, 2004, pp. 237–247.

[49] Venkatakrishnan, L., "Density Measurements in an Axisymmetric Underexpanded Jet by Background-Oriented Schlieren Technique," *AIAA Journal*, Vol. 43, No. 7, 2005, pp. 1574–1579. https://doi.org/10.2514/1.12647.

[50] Venkatakrishnan, L., and Suriyanarayanan, P., "Density field of supersonic separated flow past an afterbody nozzle using tomographic reconstruction of BOS data," *Experiments in Fluids*, Vol. 47, 2009, pp. 463–473.

[51] Sourgen, F., Leopold, F., and Klatt, D., "Reconstruction of the density field using the colored background oriented schlieren technique (CBOS)," *Optics and Lasers in Engineering*, Vol. 50, No. 1, 2012, pp. 29–38.

[52] Hartmann, U., Adamczuk, R., and Seume, J., "Tomographic background oriented schlieren applications for turbomachinery," *53rd AIAA Aerospace Sciences Meeting*, 2015, p. 1690.

[53] Atcheson, B., Ihrke, I., Heidrich, W., Tevs, A., Bradley, D., Magnor, M., and Seidel, H.-P., "Time-resolved 3D capture of non-stationary gas flows," *ACM Transactions on Graphics*, Vol. 27, No. 5, 2008, pp. 1–9. https://doi.org/10.1145/1409060.1409085.

[54] Faris, G. W., and Byer, R. L., "Three-dimensional beam-deflection optical tomography of a supersonic jet," *Applied Optics*, Vol. 27, No. 24, 1988, pp. 5202–5212.

[55] Schwarz, A., "Multi-tomographic flame analysis with a schlieren apparatus," *Measurement Science and Technology*, Vol. 7, No. 3, 1996, p. 406.

[56] Unterberger, A., and Mohri, K., "Evolutionary background-oriented schlieren tomography with self-adaptive parameter heuristics," *Optics Express*, Vol. 30, No. 6, 2022, pp. 8592–8614.

[57] Nicolas, F., Todoroff, V., Plyer, A., Le Besnerais, G., Donjat, D., Micheli, F., Champagnat, F., Cornic, P., and Le Sant, Y., "A direct approach for instantaneous 3D density field reconstruction from background-oriented schlieren (BOS) measurements," *Experiments in Fluids*, Vol. 57, 2016, pp. 1–21.

[58] Grauer, S. J., Unterberger, A., Rittler, A., Daun, K. J., Kempf, A. M., and Mohri, K., "Instantaneous 3D flame imaging by background-oriented schlieren tomography," *Combustion and Flame*, Vol. 196, 2018, pp. 284–299. https://doi.org/10.1016/j.combustflame.2018.06.022.

[59] Hu, W., Yang, L., Zhang, Y., Wang, P., and Li, J., "Reconstruction refinement of hybrid background-oriented schlieren tomography," *Physics of Fluids*, Vol. 36, No. 2, 2024.

[60] Sipkens, T. A., Grauer, S. J., Steinberg, A. M., Rogak, S. N., and Kirchen, P., "New transform to project axisymmetric deflection fields along arbitrary rays," *Measurement Science and Technology*, Vol. 33, No. 3, 2021, p. 035201.

[61] Xiong, Y., Kaufmann, T., and Noiray, N., "Towards robust BOS measurements for axisymmetric flows," *Experiments in Fluids*, Vol. 61, No. 8, 2020, p. 178.

[62] Molnar, J. P., Venkatakrishnan, L., Schmidt, B. E., Sipkens, T. A., and Grauer, S. J., "Estimating density, velocity, and pressure fields in supersonic flows using physics-informed BOS," *Experiments in Fluids*, Vol. 64, No. 1, 2023. https://doi.org/10.1007/s00348-022-03554-y.

[63] Grauer, S. J., Mohri, K., Yu, T., Liu, H., and Cai, W., "Volumetric emission tomography for combustion processes," *Progress in Energy and Combustion Science*, Vol. 94, 2023, p. 101024.

[64] Kak, A. C., and Slaney, M., *Principles of Computerized Tomographic Imaging*, SIAM, 2001.

[65] Cai, H., Song, Y., Ji, Y., Li, Z., and He, A., "Direct background-oriented schlieren tomography using radial basis functions," *Optics Express*, Vol. 30, No. 11, 2022, pp. 19100–19120.

[66] Hansen, P. C., *Rank-deficient and Discrete Ill-posed Problems: Numerical Aspects of Linear Inversion*, SIAM, 1998.

[67] Daun, K. J., Grauer, S. J., and Hadwin, P. J., "Chemical species tomography of turbulent flows: Discrete ill-posed and rank deficient problems and the use of prior information," *Journal of Quantitative Spectroscopy and Radiative Transfer*, Vol. 172, 2016, pp. 58–74.

[68] Léon, O., Donjat, D., Olchewsky, F., Desse, J.-M., Nicolas, F., and Champagnat, F., "Three-dimensional density field of a screeching under-expanded jet in helical mode using multi-view digital holographic interferometry," *Journal of Fluid Mechanics*, Vol. 947, 2022, p. A36.

[69] Yu, T., Cai, W., and Liu, Y., "Rapid tomographic reconstruction based on machine learning for time-resolved combustion diagnostics," *Review of scientific instruments*, Vol. 89, No. 4, 2018.

[70] Yu, T., Cai, W., and Liu, Y., "Rapid tomographic reconstruction based on machine learning for time-resolved combustion diagnostics," *Review of Scientific Instruments*, Vol. 89, No. 4, 2018.

[71] Wu, D., Kim, K., and Li, Q., "Computationally efficient deep neural network for computed tomography image reconstruction," *Medical Physics*, Vol. 46, No. 11, 2019, pp. 4763–4776.

[72] Bo, L., Cai, H., Song, Y., Ji, Y., Li, Z., and He, A., "Background-oriented Schlieren tomography using gated recurrent unit," *Optics Express*, Vol. 31, No. 23, 2023, pp. 39182–39200.

[73] Sun, Y., Liu, J., Xie, M., Wohlberg, B., and Kamilov, U. S., "CoIL: Coordinate-based internal learning for tomographic imaging," *IEEE Transactions on Computational Imaging*, Vol. 7, 2021, pp. 1400–1412. https://doi.org/10.1109/TCI.2021.3125564.

[74] Zhang, K., Luan, F., Wang, Q., Bala, K., and Snavely, N., "PhySG: Inverse rendering with spherical gaussians for physics-based material editing and relighting," *Proceedings of the IEEE/CVF Conference on Computer Vision and Pattern Recognition*, 2021, pp. 5453–5462. https://doi.org/10.1109/CVPR46437.2021.00541.

[75] Zang, G., Idoughi, R., Li, R., Wonka, P., and Heidrich, W., "IntraTomo: self-supervised learning-based tomography via sinogram synthesis and prediction," *Proceedings of the IEEE/CVF International Conference on Computer Vision*, 2021, pp. 1960–1970. https://doi.org/10.1109/ICCV48922.2021.00197.

[76] Rückert, D., Wang, Y., Li, R., Idoughi, R., and Heidrich, W., "NeAT: Neural adaptive tomography," *ACM Transactions on Graphics*, Vol. 41, No. 4, 2022, pp. 1–13. https://doi.org/10.1145/3528223.3530121.

[77] Molnar, J. P., LaLonde, E. J., Combs, C. S., Léon, O., Donjat, D., and Grauer, S. J., "Forward and inverse modeling of depth-of-field effects in background-oriented schlieren," *AIAA Journal*, Vol. 62, No. 11, 2024, pp. 4316–4329.

[78] He, Y., Zheng, Y., Xu, S., Liu, C., Peng, D., Liu, Y., and Cai, W., "Neural refractive index field: Unlocking the Potential of Background-oriented Schlieren Tomography in Volumetric Flow Visualization," *arXiv preprint arXiv:2409.14722*, 2024.

[79] Li, J., Meng, X., Xiong, Y., Jia, T., Pan, C., and Wang, J., "NeDF: neural deflection fields for sparse-view tomographic background oriented Schlieren," *arXiv preprint arXiv:2409.19971*, 2024.

[80] Wang, S., Sankaran, S., Wang, H., and Perdikaris, P., "An expert's guide to training physics-informed neural networks," *arXiv preprint arXiv:2308.08468*, 2023.

[81] Liu, H., Shui, C., and Cai, W., "Time-resolved three-dimensional imaging of flame refractive index via endoscopic background-oriented Schlieren tomography using one single camera," *Aerospace Science and Technology*, Vol. 97, 2020, p. 105621.

[82] Bathel, B. F., Weisberger, J. M., Ripley, W. H., and Jones, S. B., "Preparations for Tomographic Background-Oriented Schlieren at the 31-Inch Mach 10Wind Tunnel," *AIAA Aviation 2022 Forum*, 2022. https://doi.org/10.2514/6.2022-3475.

[83] Takahashi, H., Oki, J., Hirotani, T., and Taguchi, H., "Tomographic Reconstruction of Hypersonic Aircraft Flowfields in Large-Scale Wind Tunnel Experiments," *AIAA Journal*, Vol. 62, No. 3, 2024, pp. 869–881.

[84] Gupta, A., Miller, R., Bell, K., Langner, D., and Agrawal, A. K., "Quantitative Measurements in the Exhaust Flow of a Rotating Detonation Combustor Using Rainbow Schlieren Deflectometry," *Journal of Engineering for Gas Turbines and Power*, Vol. 146, No. 12, 2024.

[85] Gomez, M., Grauer, S. J., Ludwigsen, J., Steinberg, A. M., Son, S. F., Roy, S., and Meyer, T. R., "Megahertz-rate background-oriented schlieren tomography in post-detonation blasts," *Applied Optics*, Vol. 61, No. 10, 2022, pp. 2444–2458.

[86] Martins, F. J., Foo, C. T., Unterberger, A., Karaminejad, S., Endres, T., and Mohri, K., "Analyzing 3D fields of refractive index, emission and temperature in spray-flame nanoparticle synthesis via tomographic imaging using multi-simultaneous measurements (TIMes)," *Applications in Energy and Combustion Science*, Vol. 16, 2023, p. 100213.

[87] Nicolas, F., Donjat, D., Plyer, A., Champagnat, F., Le Besnerais, G., Micheli, F., Cornic, P., Le Sant, Y., and Deluc, J., "Experimental study of a co-flowing jet in ONERA's F2 research wind tunnel by 3D background oriented schlieren," *Measurement Science and Technology*, Vol. 28, No. 8, 2017, p. 085302.

[88] Akamine, M., Teramoto, S., and Okamoto, K., "Microphones and Three-dimensional Background-Oriented Schlieren Measurements of an Ideally Expanded Supersonic Jet," *AIAA SCITECH 2024 Forum*, 2024, p. 2101.

[89] Lanzillotta, L., Léon, O., Donjat, D., and Le Besnerais, G., "3D density reconstruction of a screeching supersonic jet by synchronized multi-camera Background Oriented Schlieren," *EUCASS 2019*, 2019.

[90] Amjad, S., Karami, S., Soria, J., and Atkinson, C., "Assessment of three-dimensional density measurements from tomographic background-oriented schlieren (BOS)," *Measurement Science and Technology*, Vol. 31, No. 11, 2020. https://doi.org/10.1088/1361-6501/ab955a.

[91] Hayase, T., "Numerical simulation of real-world flows," *Fluid Dynamics Research*, Vol. 47, No. 5, 2015, p. 051201.

[92] Davami, J., Juliano, T. J., Scholten, A., Paredes, P., Benitez, E. K., Running, C. L., Dylewicz, K., Pezlar, V., Theofilis, V., Thiele, T., and Willems, S., "Separation and Transition on the ROTEX-T Cone-Flare," *AIAA SCITECH 2024 Forum*, 2024, p. 0499.

[93] Ali, M. Y. B., Léon, O., Donjat, D., Bézard, H., Laroche, E., Mons, V., and Champagnat, F., "Data assimilation for aerothermal mean flow reconstruction using aero-optical observations: a synthetic investigation," *56 th 3AF International Conference on Applied Aerodynamics*, 2022.

[94] Vinnichenko, N. A., Plaksina, Y. Y., Pushtaev, A. V., and Uvarov, A. V., "Obtaining velocity and pressure distributions in natural convection flows using experimental temperature fields," *Applied Thermal Engineering*, Vol. 215, 2022, p. 118962.

[95] Raissi, M., Perdikaris, P., and Karniadakis, G. E., "Physics-informed neural networks: A deep learning framework for solving forward and inverse problems involving nonlinear partial differential equations," *Journal of Computational physics*, Vol. 378, 2019, pp. 686–707.

[96] Cai, S., Li, H., Zheng, F., Kong, F., Dao, M., Karniadakis, G. E., and Suresh, S., "Artificial intelligence velocimetry and microaneurysm-on-a-chip for three-dimensional analysis of blood flow in physiology and disease," *Proceedings of the National Academy of Sciences*, Vol. 118, No. 13, 2021. https://doi.org/10.1073/pnas.2100697118.

[97] Molnar, J. P., Venkatakrishnan, L., Schmidt, B. E., Sipkens, T. A., and Grauer, S. J., "Estimating density, velocity, and pressure fields in supersonic flows using physics-informed BOS," *Experiments in Fluids*, Vol. 64, No. 1, 2023, p. 14.

[98] Sims, J. L., *Tables for Supersonic Flow Around Right Circular Cones at Zero Angle of Attack*, Vol. 3004, Office of Scientific and Technical Information, National Aeronautics and Space Administration, 1964.

[99] Molnar, J. P., Grauer, S. J., Léon, O., Donjat, D., and Nicolas, F., "Physics-informed background-oriented schlieren of turbulent underexpanded jets," *AIAA SciTech 2023 Forum*, 2023, p. 2441.

[100] Rohlfs, L., and Weiss, J., "Assimilating mean velocity fields of a shockwave–boundary layer interaction from background-oriented schlieren measurements using physics-informed neural networks," *Physics of Fluids*, Vol. 36, No. 7, 2024.

[101] Lyu, Z., Cai, W., and Liu, Y., "An event-triggered background-oriented schlieren technique combined with dynamic projection using dynamic mirror device," *Measurement Science and Technology*, Vol. 35, No. 10, 2024. https://doi.org/10.1088/1361-6501/ad6172.

[102] Lyu, Z., Cai, W., and Liu, Y., "Event-triggered background-oriented schlieren: high-frequency visualization of a heated jet flow," *Optics Letters*, Vol. 49, No. 10, 2024. https://doi.org/10.1364/ol.515700.

[103] Shiba, S., Hamann, F., Aoki, Y., and Gallego, G., "Event-Based Background-Oriented Schlieren," *IEEE Transactions on Pattern Analysis and Machine Intelligence*, Vol. 46, No. 4, 2024, pp. 2011–2026. https://doi.org/10.1109/tpami.2023.3328188.

[104] Borer, D., Delbruck, T., and Rösgen, T., "Three-dimensional particle tracking velocimetry using dynamic vision sensors," *Experiments in Fluids*, Vol. 58, No. 12, 2017. https://doi.org/10.1007/s00348-017-2452-5.

[105] Rusch, A., and Rösgen, T., "TrackAER: real-time event-based quantitative flow visualization," *Experiments in Fluids*, Vol. 64, No. 8, 2023. https://doi.org/10.1007/s00348-023-03673-0.

[106] Willert, C. E., and Klinner, J., "Event-based imaging velocimetry: an assessment of event-based cameras for the measurement of fluid flows," *Experiments in Fluids*, Vol. 63, No. 6, 2022. https://doi.org/10.1007/s00348-022-03441-6.

[107] Willert, C. E., "Event-based imaging velocimetry using pulsed illumination," *Experiments in Fluids*, Vol. 64, No. 5, 2023. https://doi.org/10.1007/s00348-023-03641-8.

[108] Sommersel, O. K., Bjerketvedt, D., Christensen, S. O., Krest, O., and Vaagsaether, K., "Application of background oriented schlieren for quantitative measurements of shock waves from explosions," *Shock Waves*, Vol. 18, 2008, pp. 291–297. https://doi.org/10.1007/s00193-008-0142-1.

[109] Mizukaki, T., Wakabayashi, K., Matsumaura, T., and Nakayama, N., "Background-oriented schlieren with natural background for quantitative visualization of open-air explosions," *Shock Waves*, Vol. 24, 2014, pp. 69–78.

[110] Hargather, M. J., "Background-oriented schlieren diagnostics for large-scale explosive testing," *Shock Waves*, Vol. 23, 2013, pp. 529–536. https://doi.org/10.1007/s00193-013-0446-7.

[111] Mizukaki, T., "Visualization of compressible vortex rings using the background-oriented schlieren method," *Shock Waves*, Vol. 20, No. 6, 2010, pp. 531–537. https://doi.org/10.1007/s00193-010-0284-9.

[112] Stasicki, B., Hiller, W. J., and Meier, G. E. A., "High frequency stroboscope using LED light source," *Technisches Messen*, Vol. 51, No. 6, 1984, pp. 217–220. https://doi.org/10.1524/teme.1984.51.6.217.

[113] Stasicki, B., Hiller, W. J., and Meier, G. E. A., "A Light Pulse Generator For High Speed Photography Using Semiconductor Devices As A Light Source," *18th Intl Congress on High Speed Photography and Photonics*, 1989. https://doi.org/10.1117/12.969229.

[114] Willert, C. E., Mitchell, D. M., and Soria, J., "An assessment of high-power light-emitting diodes for high frame rate schlieren imaging," *Experiments in Fluids*, Vol. 53, No. 2, 2012, pp. 413–421.

[115] Stasicki, B., Schröder, A., Boden, F., and Ludwikowski, K., "High-power LED light sources for optical measurement systems operated in continuous and overdriven pulsed modes," *Optical Measurement Systems for Industrial Inspection X*, 2017. https://doi.org/10.1117/12.2270304.

[116] Parziale, N. J., Damazo, J. S., Schmidt, B. E., Wang, P. S., Hornung, H. G., and Shepherd, J. E., "Pulsed Laser Diode for use as a Light Source for Short-Exposure, High-Frame-Rate Flow Visualization," *AIAA SciTech 2015 Forum*, AIAA, 2015. https://doi.org/10.2514/6.2015-0530.

[117] Agrež, V., Požar, T., and Petkovšek, R., "High-speed photography of shock waves with an adaptive illumination," *Optics Letters*, Vol. 45, No. 6, 2020. https://doi.org/10.1364/ol.388444.

[118] Kushner, L. K., Heineck, J. T., Storms, B. L., and Childs, R., "Visualization of a Sweeping Jet by Laser Speckle Retro-reflective Background Oriented Schlieren," *53rd AIAA Aerospace Sciences Meeting*, 2015. https://doi.org/10.2514/6.2015-1697.

[119] Meier, A. H., and Roesgen, T., "Improved background oriented schlieren imaging using laser speckle illumination," *Experiments in Fluids*, Vol. 54, No. 6, 2013. https://doi.org/10.1007/s00348-013-1549-8.

[120] Weilenmann, M., Xiong, Y., Bothien, M., and Noiray, N., "Background-Oriented Schlieren of Fuel Jet Flapping Under Thermoacoustic Oscillations in a Sequential Combustor," *Journal of Engineering for Gas Turbines and Power*, Vol. 141, No. 1, 2018. https://doi.org/10.1115/1.4041240.

[121] Zhou, T., Gaskins, J., Swaine, S., Bane, S. P., Poggie, J., and Blaisdell, G. A., "High Magnification Telecentric Background Oriented Schlieren (BOS) and its Application to a Supersonic Turbulent Boundary Layer," *AIAA Scitech 2023 Forum*, 2023. https://doi.org/10.2514/6.2023-2437.

[122] Zhou, T., Gaskins, J., Poggie, J., and Bane, S. P. M., "Optimization of optical systems for background oriented schlieren," *Measurement Science and Technology*, Vol. 36, No. 1, 2024. https://doi.org/10.1088/1361-6501/ad8944.

[123] Heineck, J. T., Schairer, E. T., Walker, L. A., and Kushner, L. K., "Retroreflective background oriented schlieren (RBOS)," *14th International Symposium on Flow Visualization*, 2010.

[124] O'Brien, D. M., Mitchell, R. M., Edwards, M., and Elsum, C. C., "Estimation of BRDF from AVHRR Short-Wave Channels: Tests over semiarid Australian sites," *Remote Sensing of Environment*, Vol. 66, No. 1, 1998, pp. 71–86. https://doi.org/10.1016/s0034-4257(98)00048-0.

[125] Belcour, L., Pacanowski, R., Delahaie, M., Laville-Geay, A., and Eupherte, L., "Bidirectional reflectance distribution function measurements and analysis of retroreflective materials," *Journal of the Optical Society of America A*, Vol. 31, No. 12, 2014. https://doi.org/10.1364/josaa.31.002561.

[126] Bathel, B. F., Borg, S. E., Walker, E., and Mizukaki, T., "Development of Background-Oriented Schlieren for NASA Langley Research Center Ground Test Facilities (Invited)," *53rd AIAA Aerospace Sciences Meeting*, 2015. https://doi.org/10.2514/6.2015-1691.

[127] Weisberger, J. M., Bathel, B. F., Jones, S. B., Woike, M. R., Ponder, J. D., Heineck, J. T., and Schairer, E. T., "Preparations for Tomographic Background-Oriented Schlieren Measurements in the 11-by 11-Foot Transonic Wind Tunnel," *AIAA Aviation 2020 Forum*, AIAA, 2020, p. 3102. https://doi.org/10.2514/6.2020-3102.

[128] Weisberger, J. M., and Bathel, B. F., "Projection background-oriented schlieren," *Applied Optics*, Vol. 61, No. 20, 2022. https://doi.org/10.1364/ao.458770.

[129] Dewey, J. M., McMillin, D. J., and Classen, D. F., "Photogrammetry of spherical shocks reflected from real and ideal surfaces," *Journal of Fluid Mechanics*, Vol. 81, 1977, pp. 701–717. https://doi.org/10.1017/S0022112077002304.

[130] Dewey, J. M., *Handbook of Shock Waves*, Elsevier, 2001, Chaps. Chapter 13.1 - Spherical Shock Waves: 13.1 Expanding Spherical Shocks (Blast Waves), pp. 441–481.

[131] Dewey, J. M., *Frontiers of Shock Wave Research*, Springer, 2022, Chap. The Background of My Studies of shock and Blast Waves. https://doi.org/10.1007/978-3-030-90735-8_3.

[132] Hargather, M. J., and Settles, G. S., "Natural-background-oriented schlieren," *Experiments in Fluids*, Vol. 48, 2010, pp. 59–68. https://doi.org/10.1007/s00348-009-0709-3.

[133] Winter, K. O., and Hargather, M. J., "Three-dimensional shock wave reconstruction using multiple high-speed digital cameras and background-oriented schlieren imaging," *Experiments in Fluids*, Vol. 60, No. 6, 2019. https://doi.org/10.1007/s00348-019-2738-x.

[134] Gregoire, Y., Sturtzer, M. O., Khasainov, B. A., and Veyssiere, B., "Cinematographic investigations of the explosively driven dispersion and ignition of solid particles," *Shock Waves*, Vol. 24, 2014, pp. 393–402. https://doi.org/10.1007/s00193-014-0500-0.

[135] Pontalier, Q., Loiseau, J., Goroshin, S., and Frost, D. L., "Experimental investigation of blast mitigation and particle–blast interaction during the explosive dispersal of particles and liquids," *Shock waves*, Vol. 28, No. 3, 2018, pp. 489–511. https://doi.org/10.1007/s00193-018-0821-5.

[136] Steward, B. J., Gross, K. C., and Perram, G. P., "Optical characterization of large caliber muzzle blast waves," *Propellants Explosives Pyrotechnics*, Vol. 36, No. 6, 2011, pp. 564–575.

[137] Venkatakrishnan, L., Suriyanarayanan, P., and Jagadeesh, G., "Density field visualization of a micro-explosion using background oriented schlieren," *Journal of Visualization*, Vol. 16, 2013, pp. 177–180. https://doi.org/10.1007/s12650-013-0164-3.

[138] Yamamoto, S., Tagawa, Y., and Kameda, M., "Application of background-oriented schlieren (BOS) technique to a laser-induced underwater shock wave," *Experiments in Fluids*, Vol. 56, 2015, p. 93. https://doi.org/10.1007/s00348-015-1960-4.

[139] Strebe, K. M., "Quantitative background-oriented schlieren (BOS) measurements of explosives and high-speed projectiles using optical flow techniques," Master's thesis, New Mexico Institute of Mining and Technology, August 2023.

[140] Bauknecht, A., Merz, C. B., and Raffel, M., "Airborne visualization of helicopter blade tip vortices," *Journal of Visualization*, Vol. 20, No. 1, 2016, pp. 139–150. https://doi.org/10.1007/s12650-016-0389-z.

[141] Hill, M. A., and Haering, E. A., "Ground-to-air flow visualization using Solar Calcium-K line Background-Oriented Schlieren," *Experiments in Fluids*, Vol. 58, No. 1, 2016. https://doi.org/10.1007/s00348-016-2285-7.

[142] Bauknecht, A., Ewers, B., Wolf, C., Leopold, F., Yin, J., and Raffel, M., "Three-dimensional reconstruction of helicopter blade–tip vortices using a multi-camera BOS system," *Experiments in Fluids*, Vol. 56, No. 1, 2014. https://doi.org/10.1007/s00348-014-1866-6.

[143] Meyn, L. A., and Bennett, M. S., "Application of a Two Camera Video Imaging System to Three-Dimensional Vortex Tracking in the 80- by 120-Foot Wind Tunnel," *AIAA Applied Aerodynamics Conference*, 1993.

[144] Raffel, M., Heineck, J. T., Schairer, E., Leopold, F., and Kindler, K., "Background-Oriented Schlieren Imaging for Full-Scale and In-Flight Testing," *Journal of the American Helicopter Society*, Vol. 59, No. 1, 2014. https://doi.org/10.4050/jahs.59.012002.

[145] Gardner, A., Raffel, M., Schwarz, C., Braukmann, J., and Wolf, C. C., "Reference-free Digital Shadowgraphy Using a Moving BOS Background," *Experiments in Fluids*, Vol. 61, 2020. https://doi.org/10.1007/s00348-019-2865-4.

[146] Raffel, M., Smith, N., Wolf, C. C., Heineck, J., and Gardner, A., "Projected moving patterns for reference-free background-oriented schlieren technique (BOS)," *Measurement Science and Technology*, Vol. 35, 2024. https://doi.org/10.1088/1361-6501/ad7165.

[147] Smith, N. T., Heineck, J. T., and Schairer, E. T., "Optical Flow for Flight and Wind Tunnel Background Oriented Schlieren Imaging," *55th AIAA Aerospace Sciences Meeting*, AIAA, 2017, p. 0472. https://doi.org/10.2514/6.2017-0472.

[148] Winski, C. S., Carter, M. B., Elmiligui, A. A., Pearl, J. M., Nayani, S. N., and Durston, D. A., "Computational and Experimental Study of Plume and Shock Interaction Effects on Sonic Boom in the NASA Ames 9x7 Supersonic Wind Tunnel," *2018 AIAA Aerospace Sciences Meeting*, 2018. https://doi.org/10.2514/6.2018-0331.

[149] Born, M., and Wolf, E., *Principles of Optics*, 7th ed., Cambridge University Press, 1999.

[150] Ciddor, P. E., "Refractive index of air: new equations for the visible and near infrared," *Applied Optics*, Vol. 35, No. 9, 1996, pp. 1566–1573.

[151] Gardiner Jr, W., Hidaka, Y., and Tanzawa, T., "Refractivity of combustion gases," *Combustion and Flame*, Vol. 40, 1981, pp. 213–219.